



# CHORUS

This is the accepted manuscript made available via CHORUS. The article has been published as:

## Measurements of directed, elliptic, and triangular flow in Cu + Au collisions at $\sqrt{s_{\text{NN}}}=200$ GeV

A. Adare *et al.* (PHENIX Collaboration)

Phys. Rev. C **94**, 054910 — Published 28 November 2016

DOI: [10.1103/PhysRevC.94.054910](https://doi.org/10.1103/PhysRevC.94.054910)

# Measurements of directed, elliptic, and triangular flow in Cu+Au collisions at

$$\sqrt{s_{NN}} = 200 \text{ GeV}$$

A. Adare,<sup>13</sup> C. Aidala,<sup>38,42</sup> N.N. Ajitanand,<sup>60</sup> Y. Akiba,<sup>55,56</sup> R. Akimoto,<sup>12</sup> J. Alexander,<sup>60</sup> M. Alfred,<sup>22</sup>  
K. Aoki,<sup>31,55</sup> N. Apadula,<sup>27,61</sup> H. Asano,<sup>34,55</sup> E.T. Atomssa,<sup>61</sup> T.C. Awes,<sup>51</sup> B. Azmoun,<sup>7</sup> V. Babintsev,<sup>23</sup> M. Bai,<sup>6</sup>  
X. Bai,<sup>11</sup> N.S. Bandara,<sup>41</sup> B. Bannier,<sup>61</sup> K.N. Barish,<sup>8</sup> S. Bathe,<sup>5,56</sup> V. Baublis,<sup>54</sup> C. Baumann,<sup>7</sup> S. Baumgart,<sup>55</sup>  
A. Bazilevsky,<sup>7</sup> M. Beaumier,<sup>8</sup> S. Beckman,<sup>13</sup> R. Belmont,<sup>13,42,66</sup> A. Berdnikov,<sup>58</sup> Y. Berdnikov,<sup>58</sup> D. Black,<sup>8</sup>  
D.S. Blau,<sup>33</sup> J.S. Bok,<sup>49</sup> K. Boyle,<sup>56</sup> M.L. Brooks,<sup>38</sup> J. Bryslawskij,<sup>5,8</sup> H. Buesching,<sup>7</sup> V. Bumazhnov,<sup>23</sup>  
S. Butsyk,<sup>48</sup> S. Campbell,<sup>14,27</sup> C.-H. Chen,<sup>56</sup> C.Y. Chi,<sup>14</sup> M. Chiu,<sup>7</sup> I.J. Choi,<sup>24</sup> J.B. Choi,<sup>10,\*</sup> S. Choi,<sup>59</sup>  
P. Christiansen,<sup>39</sup> T. Chujo,<sup>65</sup> V. Cianciolo,<sup>51</sup> Z. Citron,<sup>67</sup> B.A. Cole,<sup>14</sup> N. Cronin,<sup>43,61</sup> N. Crossette,<sup>43</sup>  
M. Csanád,<sup>16</sup> T. Csörgő,<sup>68</sup> T.W. Danley,<sup>50</sup> A. Datta,<sup>48</sup> M.S. Daugherty,<sup>1</sup> G. David,<sup>7</sup> K. DeBlasio,<sup>48</sup> K. Dehmelt,<sup>61</sup>  
A. Denisov,<sup>23</sup> A. Deshpande,<sup>56,61</sup> E.J. Desmond,<sup>7</sup> L. Ding,<sup>27</sup> A. Dion,<sup>61</sup> P.B. Diss,<sup>40</sup> J.H. Do,<sup>69</sup> L. D’Orazio,<sup>40</sup>  
O. Drapier,<sup>35</sup> A. Drees,<sup>61</sup> K.A. Drees,<sup>6</sup> J.M. Durham,<sup>38</sup> A. Durum,<sup>23</sup> T. Engelmore,<sup>14</sup> A. Enokizono,<sup>55,57</sup>  
S. Esumi,<sup>65</sup> K.O. Eyser,<sup>7</sup> B. Fadem,<sup>43</sup> N. Feege,<sup>61</sup> D.E. Fields,<sup>48</sup> M. Finger,<sup>9</sup> M. Finger, Jr.,<sup>9</sup> F. Fleuret,<sup>35</sup>  
S.L. Fokin,<sup>33</sup> J.E. Frantz,<sup>50</sup> A. Franz,<sup>7</sup> A.D. Frawley,<sup>18</sup> Y. Fukao,<sup>31</sup> T. Fusayasu,<sup>45</sup> K. Gainey,<sup>1</sup> C. Gal,<sup>61</sup>  
P. Gallus,<sup>15</sup> P. Garg,<sup>3</sup> A. Garishvili,<sup>63</sup> I. Garishvili,<sup>37</sup> H. Ge,<sup>61</sup> F. Giordano,<sup>24</sup> A. Glenn,<sup>37</sup> X. Gong,<sup>60</sup> M. Gonin,<sup>35</sup>  
Y. Goto,<sup>55,56</sup> R. Granier de Cassagnac,<sup>35</sup> N. Grau,<sup>2</sup> S.V. Greene,<sup>66</sup> M. Grosse Perdekamp,<sup>24</sup> Y. Gu,<sup>60</sup> T. Gunji,<sup>12</sup>  
H. Guragain,<sup>19</sup> T. Hachiya,<sup>55,56</sup> J.S. Haggerty,<sup>7</sup> K.I. Hahn,<sup>17</sup> H. Hamagaki,<sup>12</sup> H.F. Hamilton,<sup>1</sup> S.Y. Han,<sup>17</sup>  
J. Hanks,<sup>61</sup> S. Hasegawa,<sup>28</sup> T.O.S. Haseler,<sup>19</sup> K. Hashimoto,<sup>55,57</sup> R. Hayano,<sup>12</sup> X. He,<sup>19</sup> T.K. Hemmick,<sup>61</sup>  
T. Hester,<sup>8</sup> J.C. Hill,<sup>27</sup> R.S. Hollis,<sup>8</sup> K. Homma,<sup>21</sup> B. Hong,<sup>32</sup> T. Hoshino,<sup>21</sup> N. Hotvedt,<sup>27</sup> J. Huang,<sup>7,38</sup>  
S. Huang,<sup>66</sup> T. Ichihara,<sup>55,56</sup> Y. Ikeda,<sup>55</sup> K. Imai,<sup>28</sup> Y. Imazu,<sup>55</sup> M. Inaba,<sup>65</sup> A. Iordanova,<sup>8</sup> D. Isenhower,<sup>1</sup>  
A. Isinhue,<sup>43</sup> D. Ivanishchev,<sup>54</sup> B.V. Jacak,<sup>61</sup> S.J. Jeon,<sup>44</sup> M. Jezghani,<sup>19</sup> J. Jia,<sup>7,60</sup> X. Jiang,<sup>38</sup> B.M. Johnson,<sup>7,19</sup>  
K.S. Joo,<sup>44</sup> D. Jouan,<sup>52</sup> D.S. Jumper,<sup>24</sup> J. Kamin,<sup>61</sup> S. Kanda,<sup>12,31</sup> B.H. Kang,<sup>20</sup> J.H. Kang,<sup>69</sup> J.S. Kang,<sup>20</sup>  
J. Kapustinsky,<sup>38</sup> D. Kaway,<sup>41</sup> A.V. Kazantsev,<sup>33</sup> J.A. Key,<sup>48</sup> V. Khachatryan,<sup>61</sup> P.K. Khandai,<sup>3</sup> A. Khanzadeev,<sup>54</sup>  
K.M. Kijima,<sup>21</sup> C. Kim,<sup>32</sup> D.J. Kim,<sup>29</sup> E.-J. Kim,<sup>10</sup> G.W. Kim,<sup>17</sup> M. Kim,<sup>59</sup> Y.-J. Kim,<sup>24</sup> Y.K. Kim,<sup>20</sup>  
B. Kimelman,<sup>43</sup> E. Kistenev,<sup>7</sup> R. Kitamura,<sup>12</sup> J. Klatsky,<sup>18</sup> D. Kleinjan,<sup>8</sup> P. Kline,<sup>61</sup> T. Koblesky,<sup>13</sup> M. Kofarago,<sup>16</sup>  
B. Komkov,<sup>54</sup> J. Koster,<sup>56</sup> D. Kotchetkov,<sup>50</sup> D. Kotov,<sup>54,58</sup> F. Krizek,<sup>29</sup> K. Kurita,<sup>57</sup> M. Kurosawa,<sup>55,56</sup> Y. Kwon,<sup>69</sup>  
R. Lacey,<sup>60</sup> Y.S. Lai,<sup>14</sup> J.G. Lajoie,<sup>27</sup> A. Lebedev,<sup>27</sup> D.M. Lee,<sup>38</sup> G.H. Lee,<sup>10</sup> J. Lee,<sup>17,62</sup> K.B. Lee,<sup>38</sup> K.S. Lee,<sup>32</sup>  
S. Lee,<sup>69</sup> S.H. Lee,<sup>61</sup> M.J. Leitch,<sup>38</sup> M. Leitgab,<sup>24</sup> B. Lewis,<sup>61</sup> X. Li,<sup>11</sup> S.H. Lim,<sup>69</sup> M.X. Liu,<sup>38</sup> D. Lynch,<sup>7</sup>  
C.F. Maguire,<sup>66</sup> Y.I. Makdisi,<sup>6</sup> M. Makek,<sup>67,70</sup> A. Manion,<sup>61</sup> V.I. Manko,<sup>33</sup> E. Mannel,<sup>7</sup> T. Maruyama,<sup>28</sup>  
M. McCumber,<sup>13,38</sup> P.L. McGaughey,<sup>38</sup> D. McGlinchey,<sup>13,18</sup> C. McKinney,<sup>24</sup> A. Meles,<sup>49</sup> M. Mendoza,<sup>8</sup>  
B. Meredith,<sup>24</sup> Y. Miake,<sup>65</sup> T. Mibe,<sup>31</sup> A.C. Mignerey,<sup>40</sup> A. Milov,<sup>67</sup> D.K. Mishra,<sup>4</sup> J.T. Mitchell,<sup>7</sup> S. Miyasaka,<sup>55,64</sup>  
S. Mizuno,<sup>55,65</sup> A.K. Mohanty,<sup>4</sup> S. Mohapatra,<sup>60</sup> P. Montuenga,<sup>24</sup> T. Moon,<sup>69</sup> D.P. Morrison,<sup>7,†</sup> M. Moskowicz,<sup>43</sup>  
T.V. Moukhanova,<sup>33</sup> T. Murakami,<sup>34,55</sup> J. Murata,<sup>55,57</sup> A. Mwai,<sup>60</sup> T. Nagae,<sup>34</sup> S. Nagamiya,<sup>31,55</sup>  
K. Nagashima,<sup>21</sup> J.L. Nagle,<sup>13,‡</sup> M.I. Nagy,<sup>16</sup> I. Nakagawa,<sup>55,56</sup> H. Nakagomi,<sup>55,65</sup> Y. Nakamiya,<sup>21</sup>  
K.R. Nakamura,<sup>34,55</sup> T. Nakamura,<sup>55</sup> K. Nakano,<sup>55,64</sup> C. Nattrass,<sup>63</sup> P.K. Netrakanti,<sup>4</sup> M. Nishashi,<sup>21,55</sup>  
T. Niida,<sup>65</sup> S. Nishimura,<sup>12</sup> R. Nouicer,<sup>7,56</sup> T. Novák,<sup>30,68</sup> N. Novitzky,<sup>29,61</sup> A.S. Nyanin,<sup>33</sup> E. O’Brien,<sup>7</sup>  
C.A. Ogilvie,<sup>27</sup> H. Oide,<sup>12</sup> K. Okada,<sup>56</sup> J.D. Orjuela Koop,<sup>13</sup> J.D. Osborn,<sup>42</sup> A. Oskarsson,<sup>39</sup> K. Ozawa,<sup>31</sup>  
R. Pak,<sup>7</sup> V. Pantuev,<sup>25</sup> V. Papavassiliou,<sup>49</sup> I.H. Park,<sup>17,62</sup> J.S. Park,<sup>59</sup> S. Park,<sup>59</sup> S.K. Park,<sup>32</sup> S.F. Pate,<sup>49</sup>  
L. Patel,<sup>19</sup> M. Patel,<sup>27</sup> J.-C. Peng,<sup>24</sup> D.V. Perepelitsa,<sup>7,13,14</sup> G.D.N. Perera,<sup>49</sup> D.Yu. Peressounko,<sup>33</sup> J. Perry,<sup>27</sup>  
R. Petti,<sup>7,61</sup> C. Pinkenburg,<sup>7</sup> R. Pinson,<sup>1</sup> R.P. Pisani,<sup>7</sup> M.L. Purschke,<sup>7</sup> H. Qu,<sup>1</sup> J. Rak,<sup>29</sup> B.J. Ramson,<sup>42</sup>  
I. Ravinovich,<sup>67</sup> K.F. Read,<sup>51,63</sup> D. Reynolds,<sup>60</sup> V. Riabov,<sup>47,54</sup> Y. Riabov,<sup>54,58</sup> E. Richardson,<sup>40</sup> T. Rinn,<sup>27</sup>  
N. Riveli,<sup>50</sup> D. Roach,<sup>66</sup> S.D. Rolnick,<sup>8</sup> M. Rosati,<sup>27</sup> Z. Rowan,<sup>5</sup> J.G. Rubin,<sup>42</sup> M.S. Ryu,<sup>20</sup> B. Sahlmueller,<sup>61</sup>  
N. Saito,<sup>31</sup> T. Sakaguchi,<sup>7</sup> H. Sako,<sup>28</sup> V. Samsonov,<sup>47,54</sup> M. Sarsour,<sup>19</sup> S. Sato,<sup>28</sup> S. Sawada,<sup>31</sup> B. Schaefer,<sup>66</sup>  
B.K. Schmoll,<sup>63</sup> K. Sedgwick,<sup>8</sup> J. Seele,<sup>56</sup> R. Seidl,<sup>55,56</sup> Y. Sekiguchi,<sup>12</sup> A. Sen,<sup>19,27,63</sup> R. Seto,<sup>8</sup> P. Sett,<sup>4</sup>  
A. Sexton,<sup>40</sup> D. Sharma,<sup>61</sup> A. Shaver,<sup>27</sup> I. Shein,<sup>23</sup> T.-A. Shibata,<sup>55,64</sup> K. Shigaki,<sup>21</sup> M. Shimomura,<sup>27,46</sup> K. Shoji,<sup>55</sup>  
P. Shukla,<sup>4</sup> A. Sickles,<sup>7,24</sup> C.L. Silva,<sup>38</sup> D. Silvermyr,<sup>39,51</sup> B.K. Singh,<sup>3</sup> C.P. Singh,<sup>3</sup> V. Singh,<sup>3</sup> M. Skolnik,<sup>43</sup>  
M. Slunečka,<sup>9</sup> M. Snowball,<sup>38</sup> S. Solano,<sup>43</sup> R.A. Soltz,<sup>37</sup> W.E. Sondheim,<sup>38</sup> S.P. Sorensen,<sup>63</sup> I.V. Sourikova,<sup>7</sup>  
P.W. Stankus,<sup>51</sup> P. Steinberg,<sup>7</sup> E. Stenlund,<sup>39</sup> M. Stepanov,<sup>41,\*</sup> A. Ster,<sup>68</sup> S.P. Stoll,<sup>7</sup> M.R. Stone,<sup>13</sup>  
T. Sugitate,<sup>21</sup> A. Sukhanov,<sup>7</sup> T. Sumita,<sup>55</sup> J. Sun,<sup>61</sup> J. Sziklai,<sup>68</sup> A. Takahara,<sup>12</sup> A. Taketani,<sup>55,56</sup> Y. Tanaka,<sup>45</sup>  
K. Tanida,<sup>56,59</sup> M.J. Tannenbaum,<sup>7</sup> S. Tarafdar,<sup>3,66,67</sup> A. Taranenko,<sup>47,60</sup> E. Tennant,<sup>49</sup> R. Tieulent,<sup>19</sup>  
A. Timilsina,<sup>27</sup> T. Todoroki,<sup>55,65</sup> M. Tomášek,<sup>15,26</sup> H. Torii,<sup>12</sup> C.L. Towell,<sup>1</sup> R. Towell,<sup>1</sup> R.S. Towell,<sup>1</sup> I. Tserruya,<sup>67</sup>  
H.W. van Hecke,<sup>38</sup> M. Vargyas,<sup>16</sup> E. Vazquez-Zambrano,<sup>14</sup> A. Veicht,<sup>14</sup> J. Velkovska,<sup>66</sup> R. Vértesi,<sup>68</sup> M. Virius,<sup>15</sup>

V. Vrba,<sup>15,26</sup> E. Vznuzdaev,<sup>54</sup> X.R. Wang,<sup>49,56</sup> D. Watanabe,<sup>21</sup> K. Watanabe,<sup>55,57</sup> Y. Watanabe,<sup>55,56</sup>  
 Y.S. Watanabe,<sup>12,31</sup> F. Wei,<sup>49</sup> S. Whitaker,<sup>27</sup> A.S. White,<sup>42</sup> S. Wolin,<sup>24</sup> C.L. Woody,<sup>7</sup> M. Wysocki,<sup>51</sup> B. Xia,<sup>50</sup>  
 L. Xue,<sup>19</sup> S. Yalcin,<sup>61</sup> Y.L. Yamaguchi,<sup>12,61</sup> A. Yanovich,<sup>23</sup> S. Yokkaichi,<sup>55,56</sup> J.H. Yoo,<sup>32</sup> I. Yoon,<sup>59</sup>  
 Z. You,<sup>38</sup> I. Younus,<sup>36,48</sup> H. Yu,<sup>49,53</sup> I.E. Yushmanov,<sup>33</sup> W.A. Zajc,<sup>14</sup> A. Zelenski,<sup>6</sup> S. Zhou,<sup>11</sup> and L. Zou<sup>8</sup>

(PHENIX Collaboration)

<sup>1</sup>Abilene Christian University, Abilene, Texas 79699, USA

<sup>2</sup>Department of Physics, Augustana University, Sioux Falls, South Dakota 57197, USA

<sup>3</sup>Department of Physics, Banaras Hindu University, Varanasi 221005, India

<sup>4</sup>Bhabha Atomic Research Centre, Bombay 400 085, India

<sup>5</sup>Baruch College, City University of New York, New York, New York, 10010 USA

<sup>6</sup>Collider-Accelerator Department, Brookhaven National Laboratory, Upton, New York 11973-5000, USA

<sup>7</sup>Physics Department, Brookhaven National Laboratory, Upton, New York 11973-5000, USA

<sup>8</sup>University of California-Riverside, Riverside, California 92521, USA

<sup>9</sup>Charles University, Ovocný trh 5, Praha 1, 116 36, Prague, Czech Republic

<sup>10</sup>Chonbuk National University, Jeonju, 561-756, Korea

<sup>11</sup>Science and Technology on Nuclear Data Laboratory, China Institute of Atomic Energy, Beijing 102413, P. R. China

<sup>12</sup>Center for Nuclear Study, Graduate School of Science, University of Tokyo, 7-3-1 Hongo, Bunkyo, Tokyo 113-0033, Japan

<sup>13</sup>University of Colorado, Boulder, Colorado 80309, USA

<sup>14</sup>Columbia University, New York, New York 10027 and Nevis Laboratories, Irvington, New York 10533, USA

<sup>15</sup>Czech Technical University, Zikova 4, 166 36 Prague 6, Czech Republic

<sup>16</sup>ELTE, Eötvös Loránd University, H-1117 Budapest, Pázmány P. s. 1/A, Hungary

<sup>17</sup>Ewha Womans University, Seoul 120-750, Korea

<sup>18</sup>Florida State University, Tallahassee, Florida 32306, USA

<sup>19</sup>Georgia State University, Atlanta, Georgia 30303, USA

<sup>20</sup>Hanyang University, Seoul 133-792, Korea

<sup>21</sup>Hiroshima University, Kagamiyama, Higashi-Hiroshima 739-8526, Japan

<sup>22</sup>Department of Physics and Astronomy, Howard University, Washington, DC 20059, USA

<sup>23</sup>IHEP Protvino, State Research Center of Russian Federation, Institute for High Energy Physics, Protvino, 142281, Russia

<sup>24</sup>University of Illinois at Urbana-Champaign, Urbana, Illinois 61801, USA

<sup>25</sup>Institute for Nuclear Research of the Russian Academy of Sciences, prospekt 60-letiya Oktyabrya 7a, Moscow 117312, Russia

<sup>26</sup>Institute of Physics, Academy of Sciences of the Czech Republic, Na Slovance 2, 182 21 Prague 8, Czech Republic

<sup>27</sup>Iowa State University, Ames, Iowa 50011, USA

<sup>28</sup>Advanced Science Research Center, Japan Atomic Energy Agency, 2-4

Shirakata Shirane, Tokai-mura, Naka-gun, Ibaraki-ken 319-1195, Japan

<sup>29</sup>Helsinki Institute of Physics and University of Jyväskylä, P.O.Box 35, FI-40014 Jyväskylä, Finland

<sup>30</sup>Károly Róberts University College, H-3200 Gyöngyös, Mátrai út 36, Hungary

<sup>31</sup>KEK, High Energy Accelerator Research Organization, Tsukuba, Ibaraki 305-0801, Japan

<sup>32</sup>Korea University, Seoul, 136-701, Korea

<sup>33</sup>National Research Center "Kurchatov Institute", Moscow, 123098 Russia

<sup>34</sup>Kyoto University, Kyoto 606-8502, Japan

<sup>35</sup>Laboratoire Leprince-Ringuet, Ecole Polytechnique, CNRS-IN2P3, Route de Saclay, F-91128, Palaiseau, France

<sup>36</sup>Physics Department, Lahore University of Management Sciences, Lahore 54792, Pakistan

<sup>37</sup>Lawrence Livermore National Laboratory, Livermore, California 94550, USA

<sup>38</sup>Los Alamos National Laboratory, Los Alamos, New Mexico 87545, USA

<sup>39</sup>Department of Physics, Lund University, Box 118, SE-221 00 Lund, Sweden

<sup>40</sup>University of Maryland, College Park, Maryland 20742, USA

<sup>41</sup>Department of Physics, University of Massachusetts, Amherst, Massachusetts 01003-9337, USA

<sup>42</sup>Department of Physics, University of Michigan, Ann Arbor, Michigan 48109-1040, USA

<sup>43</sup>Muhlenberg College, Allentown, Pennsylvania 18104-5586, USA

<sup>44</sup>Myongji University, Yongin, Kyonggido 449-728, Korea

<sup>45</sup>Nagasaki Institute of Applied Science, Nagasaki-shi, Nagasaki 851-0193, Japan

<sup>46</sup>Nara Women's University, Kita-uoya Nishi-machi Nara 630-8506, Japan

<sup>47</sup>National Research Nuclear University, MEPhI, Moscow Engineering Physics Institute, Moscow, 115409, Russia

<sup>48</sup>University of New Mexico, Albuquerque, New Mexico 87131, USA

<sup>49</sup>New Mexico State University, Las Cruces, New Mexico 88003, USA

<sup>50</sup>Department of Physics and Astronomy, Ohio University, Athens, Ohio 45701, USA

<sup>51</sup>Oak Ridge National Laboratory, Oak Ridge, Tennessee 37831, USA

<sup>52</sup>IPN-Orsay, Univ. Paris-Sud, CNRS/IN2P3, Université Paris-Saclay, BP1, F-91406, Orsay, France

<sup>53</sup>Peking University, Beijing 100871, P. R. China

<sup>54</sup>PNPI, Petersburg Nuclear Physics Institute, Gatchina, Leningrad region, 188300, Russia

<sup>55</sup>RIKEN Nishina Center for Accelerator-Based Science, Wako, Saitama 351-0198, Japan

<sup>56</sup>RIKEN BNL Research Center, Brookhaven National Laboratory, Upton, New York 11973-5000, USA

<sup>57</sup> *Physics Department, Rikkyo University, 3-34-1 Nishi-Ikebukuro, Toshima, Tokyo 171-8501, Japan*

<sup>58</sup> *Saint Petersburg State Polytechnic University, St. Petersburg, 195251 Russia*

<sup>59</sup> *Department of Physics and Astronomy, Seoul National University, Seoul 151-742, Korea*

<sup>60</sup> *Chemistry Department, Stony Brook University, SUNY, Stony Brook, New York 11794-3400, USA*

<sup>61</sup> *Department of Physics and Astronomy, Stony Brook University, SUNY, Stony Brook, New York 11794-3800, USA*

<sup>62</sup> *Sungkyunkwan University, Suwon, 440-746, Korea*

<sup>63</sup> *University of Tennessee, Knoxville, Tennessee 37996, USA*

<sup>64</sup> *Department of Physics, Tokyo Institute of Technology, Oh-okayama, Meguro, Tokyo 152-8551, Japan*

<sup>65</sup> *Center for Integrated Research in Fundamental Science and Engineering, University of Tsukuba, Tsukuba, Ibaraki 305, Japan*

<sup>66</sup> *Vanderbilt University, Nashville, Tennessee 37235, USA*

<sup>67</sup> *Weizmann Institute, Rehovot 76100, Israel*

<sup>68</sup> *Institute for Particle and Nuclear Physics, Wigner Research Centre for Physics, Hungarian Academy of Sciences (Wigner RCP, RMKI) H-1525 Budapest 114, POBox 49, Budapest, Hungary*

<sup>69</sup> *Yonsei University, IPAP, Seoul 120-749, Korea*

<sup>70</sup> *University of Zagreb, Faculty of Science, Department of Physics, Bijenička 32, HR-10002 Zagreb, Croatia*

Measurements of anisotropic flow Fourier coefficients ( $v_n$ ) for inclusive charged particles and identified hadrons  $\pi^\pm$ ,  $K^\pm$ ,  $p$ , and  $\bar{p}$  produced at midrapidity in Cu+Au collisions at  $\sqrt{s_{NN}} = 200$  GeV are presented. The data were collected in 2012 by the PHENIX experiment at the Relativistic Heavy Ion Collider (RHIC). The particle azimuthal distributions with respect to different order symmetry planes  $\Psi_n$ , for  $n = 1, 2$ , and  $3$  are studied as a function of transverse momentum  $p_T$  over a broad range of collision centralities. Mass ordering, as expected from hydrodynamic flow, is observed for all three harmonics. The charged-particle results are compared to hydrodynamical and transport model calculations. We also compare these Cu+Au results with those in Cu+Cu and Au+Au collisions at the same  $\sqrt{s_{NN}}$ , and find that the  $v_2$  and  $v_3$ , as a function of transverse momentum, follow a common scaling with  $1/(\epsilon_n N_{\text{part}}^{1/3})$ .

PACS numbers: 25.75.Dw

---

\* Deceased

† PHENIX Co-Spokesperson: morrison@bnl.gov

‡ PHENIX Co-Spokesperson: jamie.nagle@colorado.edu

## I. INTRODUCTION

Measurements of azimuthal anisotropies of particle emission in relativistic heavy ion collisions have proven to be an essential tool in probing the properties of the quark gluon plasma (QGP) produced in such collisions. These anisotropies can be quantified [1] by the coefficients  $v_n$  in the Fourier expansion of the particle distributions with respect to symmetry planes of the same-order  $\Psi_n$  that are determined on an event-by-event basis:  $dN/d\phi \propto 1 + \sum_{n=1} 2v_n \cos(n(\phi - \Psi_n))$ , where  $n$  is the order of the harmonic,  $\phi$  is the azimuthal angle of particles of a given type, and  $\Psi_n$  is the azimuthal angle of the  $n^{\text{th}}$ -order symmetry plane. Measurements of the second harmonic, which indicates the strength of the “elliptic flow”, led to the conclusion that the QGP produced at RHIC behaves as a nearly inviscid fluid [2–6]. In the last decade, significant effort, both experimentally and theoretically, has gone towards quantifying the specific viscosity  $\eta/s$  (shear viscosity over entropy density) of the produced QGP, as well as its temperature dependence.

Elliptic flow is thought to arise from the initial spatial anisotropy in the nuclear overlap zone, which has a lenticular shape in off-center nucleus-nucleus ( $A+A$ ) collisions. This spatial anisotropy is then converted to a momentum-space anisotropy through the pressure gradients in the expanding fluid. Measurements of  $v_2$  have been performed in symmetric  $A+A$  collision for a variety of collision energies and particle species as a function of transverse momentum, rapidity, and system size [7–15]. Various scaling properties have been explored with the goal of understanding the onset of QGP formation with center-of-mass energy and how its properties may vary. The elliptic flow scaled by the corresponding initial spatial eccentricity ( $\varepsilon_2$ ) was found to follow a universal trend when plotted against the produced particle density in the transverse plane [8, 9, 15] over a broad range of center-of-mass energies. In a more recent study [12], PHENIX showed that the transverse particle density is proportional to the third root of the number of participant nucleons  $N_{\text{part}}^{1/3}$  and that scaling with  $(\varepsilon_2 N_{\text{part}}^{1/3})$  removes the remaining system-size dependencies at various center-of-mass energies.

The first-order Fourier coefficient  $v_1$ , which is a measure of the strength of the “directed flow”, has also been studied in symmetric  $A+A$  collisions over a broad range of energies [7, 8, 16–18]. Most studies focus on measurements of  $p_T$ -integrated values of  $v_1$  as a function of rapidity or pseudorapidity, and the slope of  $dv_1/dy$  at midrapidity, which may yield information on the location of a first-order phase transition in the phase diagram of nuclear matter [19]. In symmetric  $A+A$  collisions, if the nuclei are considered to be smooth spheres,  $v_1$  is an odd function with respect to (pseudo)rapidity and vanishes at midrapidity, which is consistent with the  $p_T$ -integrated measurements.

Indeed, when the nuclei are taken as smooth spheres, all odd harmonics should vanish at midrapidity. However, event-by-event fluctuations in the initial geometry can lead to nonzero odd harmonics at midrapidity [20]. Sizable values for these harmonics have been measured at both RHIC ( $v_3$ ) [21–23] and the Large Hadron Collider ( $v_3$  and  $v_5$ ) [24–26]. Evidence for a small rapidity-even component of  $v_1$  at midrapidity has also been observed [18]. The combined experimental information from odd and even flow harmonics provides much more stringent constraints on the theoretical models [27–32] and the extracted QGP properties than measurements of elliptic flow alone.

Despite the wealth of experimental data and theoretical studies, uncertainties in the energy density deposition in the initial state of the heavy ion collisions remain a limiting factor in deducing the specific viscosity of the QGP. Asymmetric collision systems, such as Cu+Au, provide opportunities to study the effect of the initial geometry on the collective flow, particularly because odd harmonics may be enhanced at midrapidity beyond the fluctuation effects.

In this paper, we present measurements of  $v_1$ ,  $v_2$ , and  $v_3$  of charged particles and identified hadrons  $\pi^\pm$ ,  $K^\pm$ ,  $p$ , and  $\bar{p}$  produced at midrapidity in Cu+Au collisions at  $\sqrt{s_{NN}} = 200$  GeV. In Sec. II we present the experimental details of the measurements, and the sources of systematic uncertainties. The results of the measurements are presented in Sec. III. In Sec. III C we compare the flow results obtained in different collision systems and explore their scaling behavior, and in Sec. III D we present comparisons to theoretical calculations. Sec. IV summarizes our findings.

## II. EXPERIMENTAL DETAILS

The PHENIX experiment is designed for the study of nuclear matter in extreme conditions using a wide variety of experimental observables. The detector, optimized for the high-multiplicity environment of ultra-relativistic heavy ion collisions, comprises two central-arm spectrometers (East and West), two muon spectrometers (at forward and backward rapidity), and a set of detectors used to determine the global properties of the collisions. Figure 1 shows a schematic diagram of the PHENIX detector for the data recorded in 2012. The upper drawing shows a beam-axis view of the two central spectrometer arms, covering the pseudorapidity region  $|\eta| < 0.35$ . The lower drawing shows a side view of the two forward-rapidity muon arms (North and South) and the global detectors. A detailed description of the complete set of detectors is given in Ref. [33].

The analysis presented here employs the global detectors, drift chamber (DC), three layers of multi-wire proportional chambers (PC1, PC2, and PC3), the time-of-flight detectors (TOFE, TOFW), and the electromagnetic calorimeter

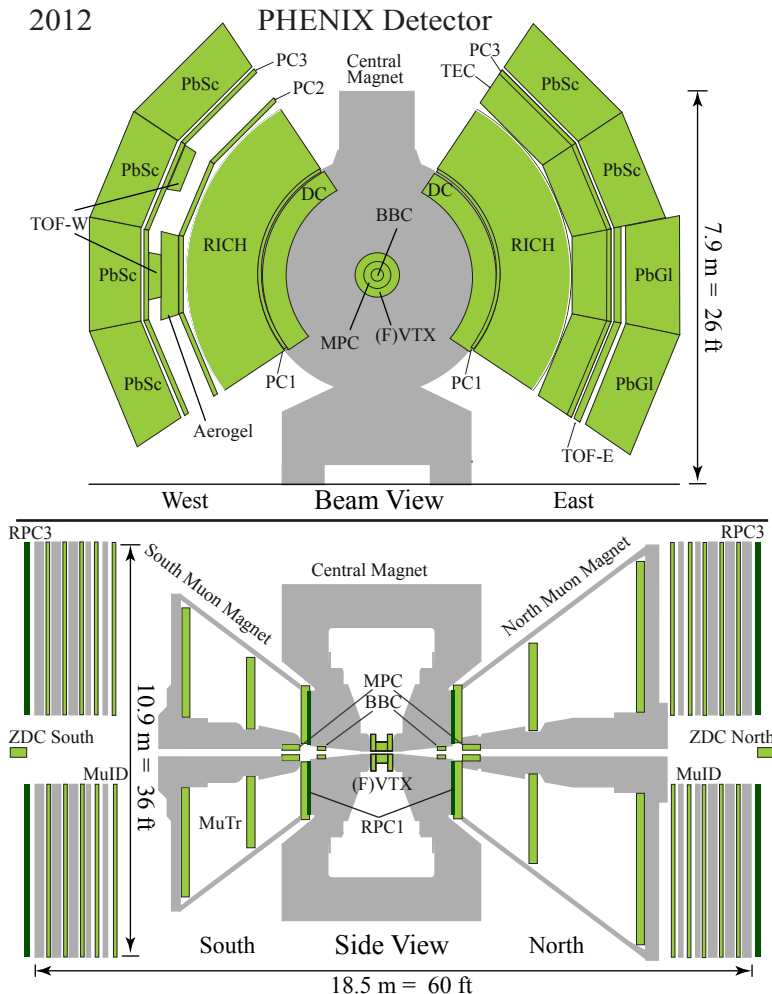


FIG. 1. (Color online) The PHENIX detector configuration for RHC Run-12 data taking period

195 (EMCal). The global system includes the beam-beam counters (BBCs), zero degree calorimeters (ZDCs) and the  
 196 shower maximum detectors (SMDs). Below, we give a brief description of each of these detector sub-systems and  
 197 their role in the present analysis.

198

### A. Global Detectors

199 The BBCs are located at  $\pm 144$  cm from the nominal interaction point along the beam line, cover  $2\pi$  in azimuth,  
 200 and span the pseudorapidity range  $3.0 < |\eta| < 3.9$ . Each BBC comprises 64 Čerenkov telescopes, arranged radially  
 201 around the beam line. The BBCs provide the main interaction trigger for the experiment and are also used in the  
 202 determination of the collision vertex position along the beam axis ( $z$ -vertex) with  $\sigma_z = 0.6$  cm resolution and the  
 203 centrality of the collisions. The event centrality class in Cu+Au collisions is determined as a percentile of the total  
 204 charge measured in the BBC from both sides. The BBCs also provide the start time for the time-of-flight measurement  
 205 with a timing resolution around  $\sigma_t = 40$  ps in central Cu+Au collisions [33].

206 The ZDCs [34] are hadronic calorimeters located forward and backward of the PHENIX detector, along the beam  
 207 line. Each ZDC is subdivided into three identical modules of two interaction lengths. They cover a pseudorapidity  
 208 range of  $|\eta| > 6.5$  and measure the energy of spectator neutrons with an energy resolution of  $\sigma(E)/E = 85\%/\sqrt{E} +$   
 209  $9.1\%$ . The SMDs [34] are scintillator strip hodoscopes located between the first and second ZDC modules, a location  
 210 corresponding approximately to the maximum of the hadronic shower. The horizontal coordinate is sampled by seven  
 211 scintillator strips of 15 mm width, while the vertical coordinate is sampled by eight strips of 20 mm width. The

212 active area of each SMD is 105 mm  $\times$  110 mm (horizontal  $\times$  vertical dimension). Scintillation light is delivered to a  
 213 multichannel Hamamatsu PMT R5900-M16 by wavelength shifting fibers [34]. A typical position resolution for SMD  
 214 is  $\sim 0.1$ – $0.3$  cm.

215

## B. Tracking and Particle Identification Detectors

216 The charged-particle momentum is reconstructed using the tracking system. This system comprises the DC, located  
 217 outside an axially-symmetric magnetic field at a radial distance between 2.0 m and 2.4 m, followed by PC1-3. The  
 218 pattern recognition in the DC is based on a combinatorial Hough transform [35] in the track bend plane. A track  
 219 model based on a field-integral look-up table determines the charged-particle momentum, the path length to the  
 220 time-of-flight detector, and a projection of the track to the outer detectors.

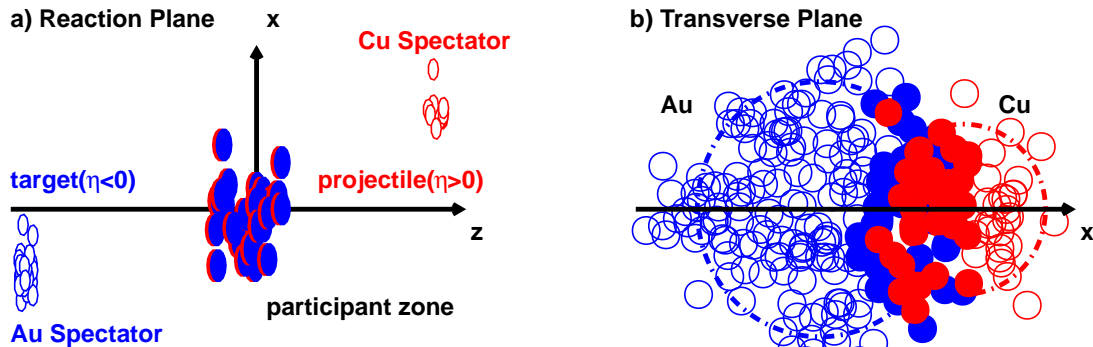


FIG. 2. (Color online) Sketch of a noncentral heavy-ion collision. See text for description of the figure.

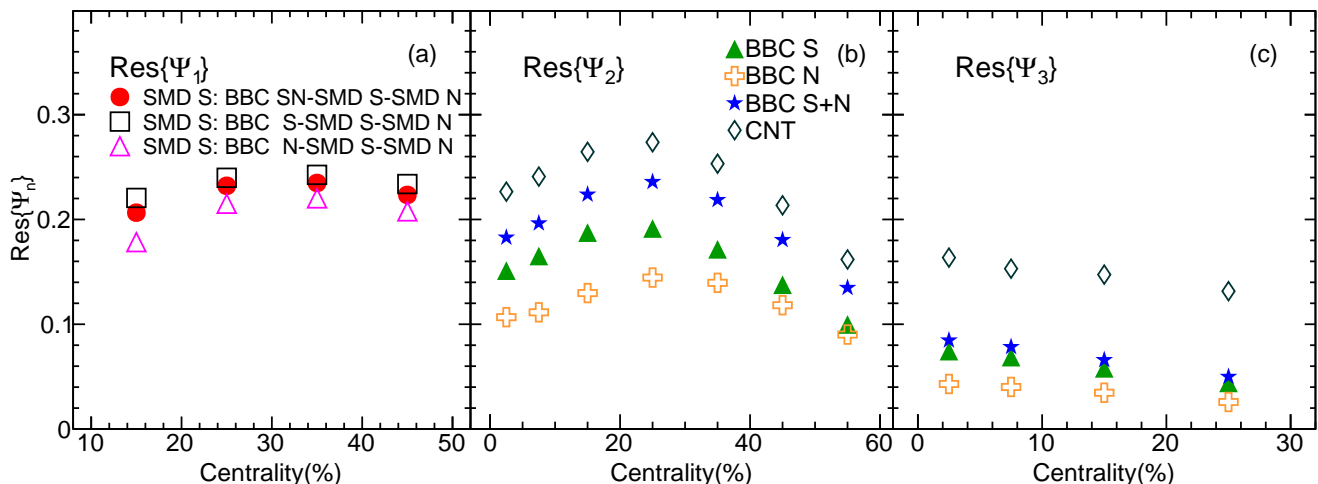


FIG. 3. (Color online) Panel (a) event-plane resolution as a function of centrality for the SMDS detectors. Panel (b) and (c) second- and third-order event-plane resolution. The BBC event-plane resolution is obtained from two sub-events and BBCS, BBCN, CNT from three sub-events as a function of centrality.

221 The tracks are matched to hits registered in the PC3 and the EMCAL, thus reducing the contribution of tracks  
 222 originating from decays and  $\gamma$ -conversions.

223 The primary particle identification detectors used in this analysis are the time-of-flight detectors. The different  
 224 detectors in the east and west arms, use different technologies (scintillators and MRPCs respectively) and have  
 225 different time resolutions [36, 37]. The total timing resolutions (including the start time measurement from the BBC)  
 226 are 130 ps and 95 ps for east and west, respectively. Pion, kaon, and (anti)proton tracks are identified with over 97%

227 purity for  $p_T < 2$  GeV/c [36, 38] in both systems. For  $p_T$  between 2–3 GeV/c, the purity of pions and protons is  
 228 about 95% and that of kaons is around 90%.

229

### C. Anisotropic Flow Measurement Technique

230 The present measurements use the event-plane method [39] to quantify the azimuthal anisotropies of the particles  
 231 produced in Cu+Au collisions. The  $v_1$ ,  $v_2$ , and  $v_3$  Fourier coefficients are determined as a function of centrality and  
 232  $p_T$  for inclusive charged particles and identified hadrons  $\pi^\pm$ ,  $K^\pm$ ,  $p$ , and  $\bar{p}$  (with charge signs combined).

233 In the event-plane method, a measured event-plane direction  $\Psi_n^{\text{obs}}$  is determined for every event and for each order  
 234  $n$ . The harmonic coefficients  $v_n\{\Psi_n\} = \langle \cos n(\phi - \Psi_n^{\text{obs}}) \rangle / \text{Res}\{\Psi_n\}$  are then measured with respect to the event  
 235 plane for each harmonic, where  $\phi$  is the azimuthal angle of the hadron and  $\text{Res}\{\Psi_n\}$  is the event-plane resolution.

236 The collision geometry of a Cu+Au collision is shown in Fig. 2(a) projected onto the reaction plane, and in  
 237 Fig. 2(b) projected onto the plane perpendicular to the beam axis. Figure 2(a) shows direction of the projectile (Cu)  
 238 and target (Au) spectators, which are bent away from the participant zone. There is an alternative picture, in which  
 239 the spectators are attracted towards the center of the system, as discussed in [40]. In this paper, we assume the  
 240 former picture for the determination of the direction of the event-plane angle from the spectators.

241 As shown in Fig. 2(a), the Cu spectators fly along the the positive-rapidity direction (North) and the Au spectators  
 242 go towards the negative-rapidity direction (South). The central position of the Au spectators is measured by the  
 243 South SMD (SMDS) to determine the spectator plane  $\Psi_1^{\text{SMDS}}$ . The  $v_1$  of charged and identified hadrons is measured  
 244 with respect to  $\Psi_1^{\text{SMDS}}$ , as indicated in Eq. 1. Measurement with respect to the spectator plane is preferred over  
 245 the first order event-plane determined by the distribution of the produced particles, because the distribution of the  
 246 spectators is less distorted by momentum conservation effects.

$$v_1 = -\langle \cos(\phi_{\text{track}} - \Psi_1^{\text{SMDS}}) \rangle / \text{Res}(\Psi_1^{\text{SMDS}}) \quad (1)$$

$$\begin{aligned} \text{Res}(\Psi_1^{\text{SMDS}}) &= \langle \cos(\Psi_1^{\text{SMDS}} - \Psi_1) \rangle \\ &= \sqrt{\frac{\langle \cos(\Psi_1^{\text{SMDS}} - \Psi_1^{\text{SMDN}}) \rangle \langle \cos(\Psi_1^{\text{SMDS}} - \Psi_1^{\text{BBCSN}}) \rangle}{\langle \cos(\Psi_1^{\text{SMDN}} - \Psi_1^{\text{BBCSN}}) \rangle}} \end{aligned} \quad (2)$$

247 There is a negative sign in Eq. 1 to keep the convention in which the direction of projectile (Cu) spectators is positive.  
 248 In Eq. 2 the resolution of  $\Psi_1^{\text{SMDS}}$  is calculated in 10% centrality intervals with the three subevent method [39, 41]  
 249 by combining the other Cu spectator plane from the North SMD (SMDN) and the first order participant event-plane  
 250 measured by the combined South and North BBCs (BBCSN). However, this method for determining the resolution  
 251 assumes a nonfluctuating nuclear-matter distribution. Event-by-event fluctuations in the initial energy density of the  
 252 collision will cause the  $v_1$  signal to be different with respect to  $\Psi_1^{\text{SMDS}}$  and  $\Psi_1^{\text{SMDN}}$  due to the rapidity-symmetric  
 253 component in the direct flow [42]. To cover this uncertainty, the resolution of  $\Psi_1^{\text{SMDS}}$  is also calculated using the  
 254 participant plane from either BBCS or BBCN and the differences are assigned as a systematic uncertainty.

255 The second ( $\Psi_2$ ) and third ( $\Psi_3$ ) order event planes are measured by the combination of BBCS and BBCN. To  
 256 determine the second and third order event-plane resolution from the BBC, we first measure the second and third  
 257 order event planes with the BBCS (Au-going side), BBCN (Cu-going side) and central arm tracks (CNT). The  
 258 central-arm tracks are restricted to low  $p_T$  ( $0.2 < p_T < 2.0$  GeV/c) to minimize the contribution from jet fragments.  
 259 The second and third order event-plane resolution of BBCS, BBCN, and CNT are calculated using three subevent  
 260 methods with a combination of BBCS-BBCN-CNT. Then the second and third order event-plane resolutions of the  
 261 BBC (including both BBCS and BBCN) are calculated with two subevent methods with a combination of BBC-CNT.

262 The event-plane resolutions for different subsystems are shown in Fig. 3 as a function of centrality. Panel (a) of  
 263 Fig. 3 shows the resolution of the first-order event plane as measured by the SMDS using three different methods.  
 264 The first method uses a three subevent combination SMDS-BBCSN-SMDN, shown with circles, the second method  
 265 shown with open squares uses a three subevent combination SMDS-BBCS-SMDN, and the third method shown with  
 266 open triangles uses the combination SMDS-BBCN-SMDN. The resolution of the second and third order event planes  
 267 for BBC, BBCS, BBCN, and CNT are shown in panel (b) and (c) of Fig. 3, respectively.

### D. Number of Participants and Eccentricity

A Monte-Carlo Glauber simulation was used to estimate the average number of participating nucleons  $N_{\text{part}}$  and the eccentricity

$$\varepsilon_n = \frac{\sqrt{\langle r^2 \cos(n\phi) \rangle^2 + \langle r^2 \sin(n\phi) \rangle^2}}{\langle r^2 \rangle} \quad (3)$$

This simulation employed a Glauber model with a Woods-Saxon density profile and includes modeling of the BBC response [43, 44]. The eccentricity defined in Eq. 3 is also known as the participant eccentricity  $\varepsilon_{\text{part}}$  and includes the effect of fluctuations from the initial participant geometry. Table I summarizes  $N_{\text{part}}$  and  $\varepsilon_n$ .

TABLE I. Number of participants and the participant eccentricity ( $\varepsilon_2$ ,  $\varepsilon_3$ ) from Monte-Carlo Glauber calculations for Au+Au, Cu+Cu and Cu+Au collisions at 200 GeV

centrality bin	Au+Au 200 GeV			Cu+Cu 200 GeV		Cu+Au 200 GeV		
	$N_{\text{part}}$	$\varepsilon_2$	$\varepsilon_3$	$N_{\text{part}}$	$\varepsilon_2$	$N_{\text{part}}$	$\varepsilon_2$	$\varepsilon_3$
0%–10%	325.2 ±3.3	0.103 ±0.003	0.087 ± 0.002	98.2 ±2.4	0.163 ±0.003	177.2 ±5.2	0.138 ±0.011	0.130 ±0.004
10%–20%	234.6 ±4.7	0.200 ±0.005	0.122 ± 0.004	73.6 ±2.5	0.241 ±0.007	132.4 ±3.7	0.204 ±0.008	0.161 ±0.005
20%–30%	166.6 ±5.4	0.284 ±0.006	0.156 ± 0.005	53.0 ±1.9	0.317 ±0.006	95.1 ±3.2	0.280 ±0.008	0.208 ±0.007
30%–40%	114.2 ±4.4	0.356 ±0.006	0.198 ± 0.008	37.3 ±1.6	0.401 ±0.008	65.7 ±3.4	0.357 ±0.010	0.266 ±0.010
40%–50%	74.4 ±3.8	0.422 ±0.006	0.253 ± 0.011	25.4 ±1.3	0.484 ±0.008	43.3 ±3.0	0.436 ±0.013	0.332 ±0.013
50%–60%	45.5 ±3.3	0.491 ±0.005	0.325 ± 0.018	16.7 ±0.9	0.579 ±0.008	26.8 ±2.6	0.523 ±0.019	0.412 ±0.019

### E. Data set

The measurements presented here use data from Cu+Au collisions at  $\sqrt{s_{NN}} = 200$  GeV collected by the PHENIX experiment at RHIC in 2012. Minimum bias events triggered by the BBC recorded within  $\pm 30$  cm from the nominal interaction point along the z-axis were used. The events were examined to ensure that stable performance is seen in the detectors used in the analysis, namely DC, PC3, TOF, BBC, and SMD. A total of  $3.6 \times 10^9$  events were analyzed.

### F. Systematic Uncertainties

TABLE II. Systematic uncertainties in the  $v_1$  measurements.

$v_1$	Uncertainty Sources	10%–20%	40%–50%	Type
$v_1$	Event-plane	20%	12%	C
	Background(absolute value)	$5 \times 10^{-4}$	$5 \times 10^{-4}$	A
	Acceptance (absolute value)	$3 \times 10^{-3}$	$2 \times 10^{-3}$	C

Tables II–V summarize the systematic uncertainties for the measurements of  $v_1$ ,  $v_2$ , and  $v_3$  for inclusive and identified charged hadrons, which are categorized by the types:

A point-to-point uncertainties uncorrelated between  $p_T$  bins;

TABLE III. Systematic uncertainties given in percent on the  $v_2$  and  $v_3$  measurements.

$v_n$ (n=2,3)	Uncertainty Sources	0%–10%	20%–30%	Type
$v_2$	Event-plane	3%	4%	B
	Background	2%	2%	A
	Acceptance	2%	3%	C
$v_3$	Event-plane	3%	7%	B
	Background	2%	2%	A
	Acceptance	8%	10%	C

TABLE IV. Systematic uncertainties in the measured  $v_1$  for identified particles.

species	$p_T \leq 2$ GeV/ $c$	$p_T \geq 2$ GeV/ $c$	Type
pion (absolute value)	$1 \times 10^{-3}$	$2 \times 10^{-3}$	A
kaon (absolute value)	$1 \times 10^{-3}$	$3 \times 10^{-3}$	A
proton (absolute value)	$1 \times 10^{-3}$	$3 \times 10^{-3}$	A

283 B  $p_T$ -correlated, all points move in a correlated manner, but not by the same factor;

284 C an overall normalization error in which all points move by the same multiplicative factor independent of  $p_T$ .

285 Contributions to the uncertainties are from the following sources:

- 286 1. event-plane resolution correction,
- 287 2. event plane as measured using different detectors,
- 288 3.  $v_n$  from background tracks,
- 289 4. acceptance dependencies
- 290 5. PID purity.

291 The uncertainties from measurements of the event planes using different detectors are found to only weakly depend  
 292 on  $p_T$ . For the measurement of  $v_1$ , the uncertainties are obtained by comparing the  $v_1$  as measured with SMDS  
 293 with alternately BBCN or BBCS used for resolution. For  $v_2$  and  $v_3$ , the uncertainties are obtained by comparing  
 294 the  $v_2$  and  $v_3$  as measured by the BBCN and BBCS. For the  $v_1$  measurement, for the 10%–20% centrality class we  
 295 find a 20% systematic uncertainty independent of  $p_T$ . For the 40%–50% centrality class, we find a 12% systematic  
 296 uncertainty. For  $v_2$ , the systematic uncertainty is less than 3% for the 0%–10% centrality range and increases to 4%  
 297 for the centrality range 50%–60%. For  $v_3$ , a 3% systematic uncertainty is found for 0%–10% centrality, increasing to  
 298 7% for the 20%–30% centrality range.

299 Background tracks that are not removed by the tracking selections as described in Sec.II may influence the measured  
 300  $v_n$ . They can arise from particle decays,  $\gamma$ -conversions, or false track reconstruction. We estimate the tracking  
 301 background contribution by varying the width of the track-matching window in PC3 and comparing the results with  
 302 and without the EMCAL matching cut. We find that the absolute uncertainty for  $v_1$  is less than  $5 \times 10^{-4}$ . For  $v_2$  and  
 303  $v_3$ , the change is less than 2%.

TABLE V. Systematic uncertainties in percent on the measured  $v_2$  and  $v_3$  for identified particles.

species	$p_T \leq 2$ GeV/ $c$	$p_T \geq 2$ GeV/ $c$	Type
pion	3%	5%	A
kaon	3%	10%	A
proton	3%	5%	A

Systematic uncertainties of acceptance were evaluated using different subsets of the detector such as DC and TOF in the east and west arms. Differences in the  $v_n$  measured using different arms may be caused by different detector alignment and performance. Maximum differences of order 3% and 10% were found for  $v_2$  and  $v_3$  respectively. These uncertainties have centrality dependence and minimal  $p_T$  dependence. For  $v_1$ , maximum absolute uncertainty of  $3 \times 10^{-3}$  is found. These uncertainties are detailed further in Tables II and III.

An additional systematic uncertainty in  $v_n$  resulting from hadron misidentification is based on the PID purity estimates from the TOF detectors as discussed in Sec.II. Pion, kaon, and proton species purity is greater than 90% and the differences between their corresponding  $v_n$  is less than a factor of two. For  $v_2$  and  $v_3$ , an additional uncertainty of 3% (type A) attributable to contamination from other species is found for particles with  $p_T < 2$  GeV/c, 5% for higher  $p_T$  pions and protons, and 10% for higher  $p_T$  kaons. In the measurements of  $v_1$ , a common absolute uncertainty of  $1 \times 10^{-3}$  is found for the three particle species for  $p_T < 2$  GeV/c, and at higher  $p_T$  the uncertainties are  $2 \times 10^{-3}$  for pions and  $3 \times 10^{-3}$  for kaons and protons, respectively. The uncertainties due to particle identification are to be added in quadrature to the values listed in Tables II and III.

### III. RESULTS AND DISCUSSION

#### A. Harmonic flow results from Cu+Au collisions

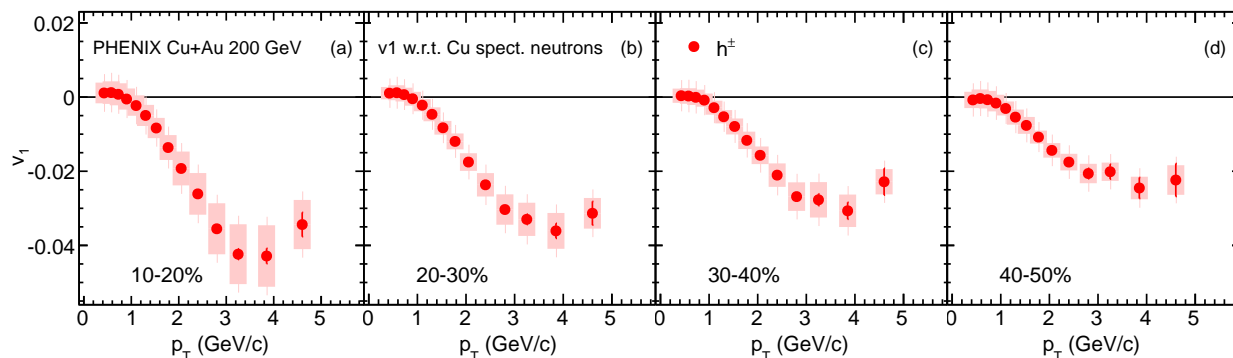


FIG. 4. (Color online)  $v_1(p_T)$  for charged hadrons measured with respect to the Cu spectator neutrons at midrapidity in Cu+Au collisions at  $\sqrt{s_{NN}} = 200$  GeV. Error bars show the statistical uncertainties, and shaded boxes indicate the systematic uncertainties.

Figures 4–6 show the  $v_1$ ,  $v_2$ , and  $v_3$  results for charge-combined hadrons measured as a function of  $p_T$  in Cu+Au collisions at  $\sqrt{s_{NN}} = 200$  GeV. Different centrality intervals are studied. The filled circles show the  $v_n(p_T)$  data, and the systematic uncertainties are shown with the shaded boxes.

The  $v_1(p_T)$  measurements shown in Fig. 4 are performed with respect to the event plane determined by spectator neutrons from the Au nucleus. To align with previous conventions, we flip the sign so that it is effectively with respect to the spectator neutrons from the Cu nucleus, as noted in Sec. II C. In all centrality intervals, high  $p_T$  particles at midrapidity move in the direction opposite of the Cu nucleus spectator neutrons, as indicated by the negative  $v_1$  values. Low  $p_T$  particles might then be expected to move in the opposite direction by conservation of momentum, and there is a hint of this effect though not beyond current systematic uncertainties. The  $v_1$  component is consistent with zero for  $p_T < 1$  GeV/c and its absolute value increases at higher  $p_T$ . The maximum of the absolute value decreases from central to peripheral collisions. This is contrary to the centrality dependence of  $v_2$  where the values increase from the most central 0%–10% collisions, up to the 30%–40% centrality class. This trend in  $v_2$  is expected from the initial geometry, because the ellipticity of the participant zone  $\varepsilon_2$  (see Table I) increases in the peripheral collisions. The  $v_2(p_T)$  values in the 30%–40%, 40%–50%, and 50%–60% Cu+Au centrality classes, shown in Fig. 5 are consistent with each other, showing very little, if any centrality dependence. The  $v_2$  and  $v_3$  values are positive, as previously observed in symmetric collisions systems. For all three harmonics, the magnitude of the signal increases with  $p_T$  up to about  $p_T = 3$  GeV/c, and then tends to decrease. This may indicate a change in the dominant production mechanism, e.g., an increasing contribution from jet fragments, or it may be due to the fact that higher  $p_T$  particles

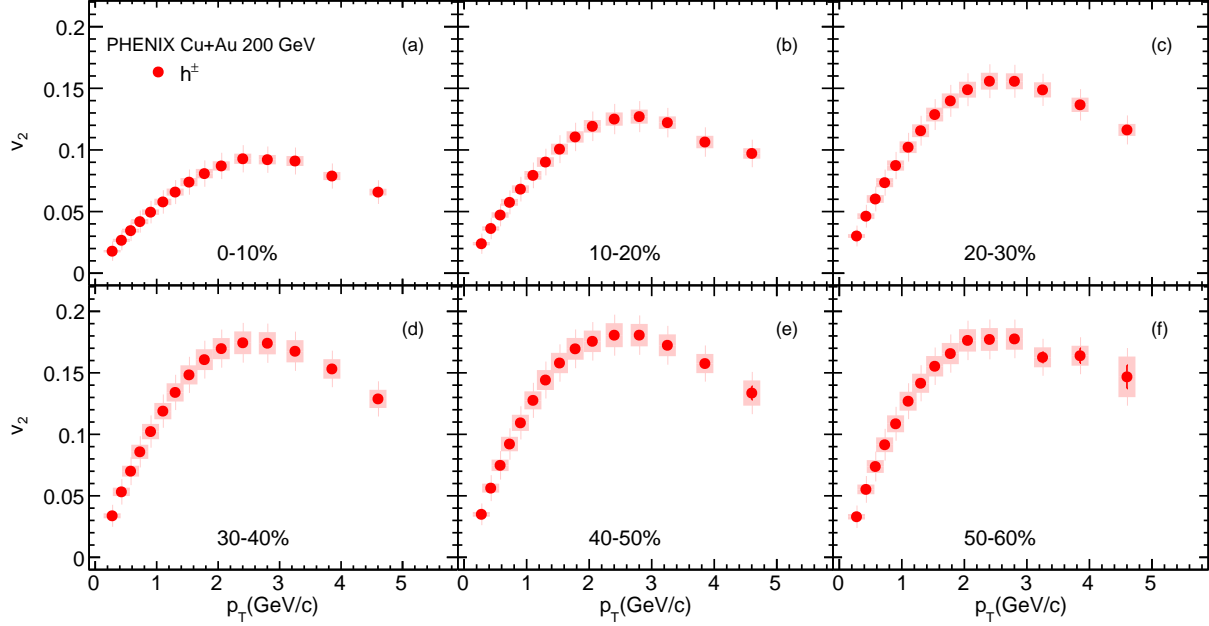


FIG. 5. (Color online)  $v_2(p_T)$  for charged hadrons measured at midrapidity in Cu+Au collisions at  $\sqrt{s_{NN}} = 200$  GeV. Uncertainties are as in Fig. 4.

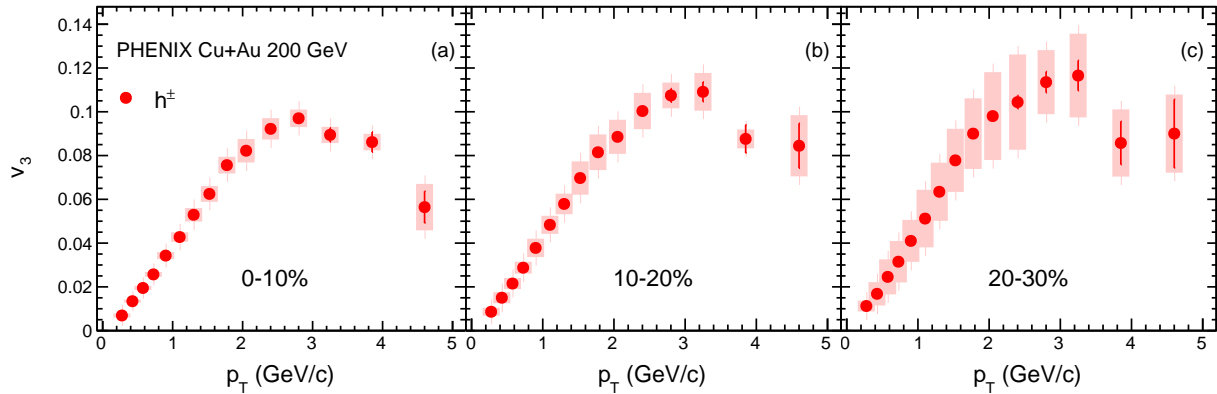


FIG. 6. (Color online)  $v_3(p_T)$  for charged hadrons measured at midrapidity in Cu+Au collisions at  $\sqrt{s_{NN}} = 200$  GeV. Uncertainties are as in Fig. 4.

337 escape the fireball with fewer interactions.

338 The  $v_3$  component (Fig. 6) has weak centrality dependence, a behavior which is similar in symmetric  $A+A$  colli-  
 339 sions [21, 22], where the triangular flow at midrapidity is completely driven by the event-by-event fluctuations of the  
 340 interaction zone. These fluctuations are also present in the asymmetric Cu+Au collisions and are expected to play a  
 341 similar role. In Sec. III C we compare the flow results obtained in different collisions systems and explore their scaling  
 342 behavior.

## B. Identified particle flow results

Figures 7 and 8 show the particle-species dependence of  $v_2$  and  $v_3$  in Cu+Au collisions. Results are presented for charge-combined  $\pi^\pm$ ,  $K^\pm$ ,  $p$ , and  $\bar{p}$ . The measured  $v_n(p_T)$  values are shown with points, and the shaded boxes represent the species-dependent type A systematic uncertainties. The type B and C systematic uncertainties shown in Table III are largely common for all particle species. For the odd harmonics, to improve the statistical significance of the results the measurements for identified particles are performed in a single centrality interval, namely 0%–30% for  $v_3(p_T)$  and 10%–50% for  $v_1(p_T)$ .

There are two trends common to both  $n = 2, 3$  results shown in Figs. 7 and 8: First, in the low- $p_T$  region the anisotropy appears largest for the lightest hadron and smallest for the heaviest hadron. A similar mass ordering is also predicted by hydrodynamics, in which all particles are moving in a common velocity field. Second, for  $p_T \geq 2$  GeV/ $c$  this mass dependence is reversed, such that the anisotropy is larger for the baryons than it is for mesons at the same  $p_T$ . These patterns have been observed previously in  $v_n$  measurements for identified particles in Au+Au collisions at RHIC. The  $v_1(p_T)$  values, presented in Fig. 9, also show mass ordering, although these measurements have larger overall systematic and statistical uncertainties than  $v_2(p_T)$  and  $v_3(p_T)$ . As in the case of  $v_1(p_T)$  for charged particles described in Sec. III (Fig. 4), we note that although the values of  $v_1(p_T)$  for each species appear to be positive at low  $p_T$ , if the full systematic uncertainty of type B and C is taken into account, a definitive conclusion can not be drawn about the overall sign of the bulk directed flow. The mass dependence in the collective flow at the low- $p_T$  is a generic feature of hydrodynamical models. The dependence on valence quark number in the intermediate- $p_T$  region has been associated with the development of flow in the partonic phase of the fireball evolution and subsequent hadronization by parton coalescence [45].

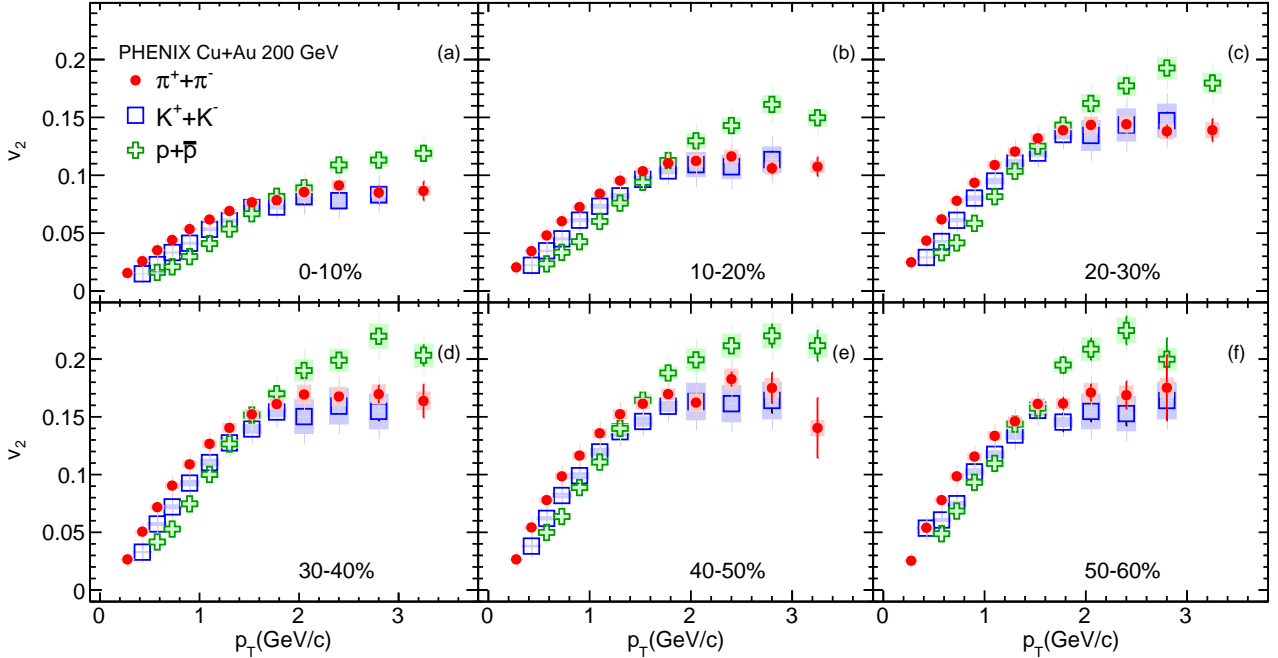


FIG. 7. (Color online) The second-order Fourier coefficients  $v_2(p_T)$  for charge-combined identified hadrons  $\pi^\pm$ ,  $K^\pm$ ,  $p$ , and  $\bar{p}$  measured at midrapidity in Cu+Au collisions at  $\sqrt{s_{NN}} = 200$  GeV for the centrality classes marked in each panel. The symbols represent the measured  $v_2(p_T)$  values, the error bars show the statistical uncertainties, and the shaded boxes indicate the systematic uncertainties from PID. The full systematic uncertainties, that are mostly common to all particle species are shown in Table III.

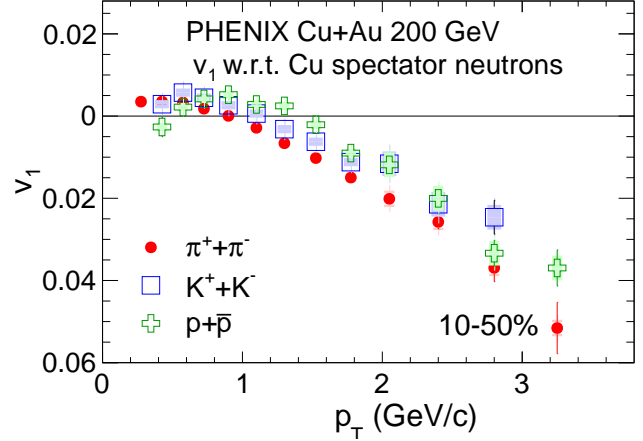
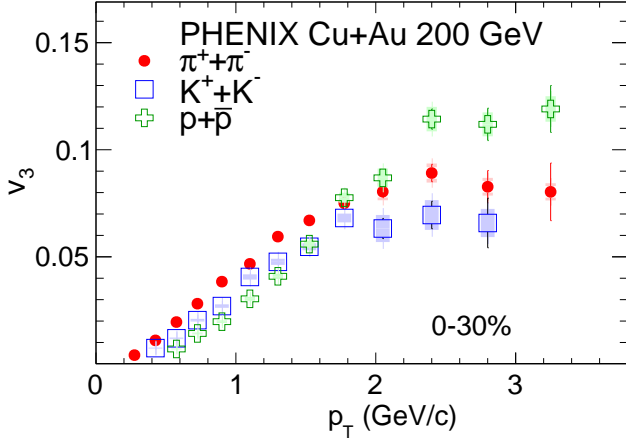


FIG. 8. (Color online) The third-order Fourier coefficients  $v_3(p_T)$  for charge-combined identified hadrons  $\pi^\pm$ ,  $K^\pm$ ,  $p$ , and  $\bar{p}$  measured at midrapidity in Cu+Au collisions at  $\sqrt{s_{NN}} = 200$  GeV for 0%–30% centrality. The symbols represent the measured  $v_3(p_T)$  values, the error bars show the statistical uncertainties, and the shaded boxes indicate the systematic uncertainties from PID. The full systematic uncertainties, that are mostly common to all particle species are shown in Table III.

FIG. 9. (Color online) The first-order Fourier coefficients  $v_1(p_T)$  for charge-combined identified hadrons  $\pi^\pm$ ,  $K^\pm$ ,  $p$ , and  $\bar{p}$  measured at midrapidity in Cu+Au collisions at  $\sqrt{s_{NN}} = 200$  GeV for 10%–50% centrality. The symbols represent the measured  $v_1(p_T)$  values with respect to the Cu spectator neutrons, the error bars show the statistical uncertainties and the shaded boxes indicate the systematic uncertainties from PID. The full systematic uncertainties, that are mostly common to all particle species are shown in Table II.

### C. System size dependence

363

364 It is interesting to compare the charged-hadron  $v_n(p_T)$  results for different collision systems measured in the  
 365 same experiment at the same center-of-mass energy. PHENIX has previously studied anisotropic flow harmonics in  
 366 symmetric Au+Au and Cu+Cu collisions at  $\sqrt{s_{NN}} = 200$  GeV [12, 22]. By varying the system size and the centrality  
 367 selection, one can study the effects of the initial geometry on the observed flow coefficients. We will first compare  
 368 the results obtained in different collision systems for the same centrality selections, and then explore possible scaling  
 369 behaviors.

370 In Fig. 10, the  $v_2(p_T)$  coefficients are compared for six different centrality selections. We observe that in each  
 371 centrality class at a given  $p_T$  the values measured in Cu+Au collisions are always between those measured in Cu+Cu  
 372 and Au+Au collisions. In all centrality classes chosen, the Cu+Cu system has larger elliptic eccentricity than both  
 373 Cu+Au and Au+Au collisions. However, except in the most central 0%–10% collisions, the measured  $v_2(p_T)$  values  
 374 are not ordered according to the magnitude of  $\varepsilon_2$  in the different systems listed in Table I. To further investigate this,  
 375 in Fig. 11 we scale the  $v_2(p_T)$  values in each collision system with their respective participant eccentricity  $\varepsilon_2$ . The  
 376 resulting  $v_2(p_T)/\varepsilon_2$  are ordered by system size, but this scaling does not lead to a universal behavior.

377 In Ref. [12], PHENIX compared measurements in Cu+Cu and Au+Au collisions for different center-of-mass energies  
 378 and centrality selections and found that the  $v_2$  values obey common empirical scaling with  $\varepsilon_2 N_{\text{part}}^{1/3}$ . The motivation  
 379 for introducing the  $N_{\text{part}}^{1/3}$  factor is that under the assumption that  $N_{\text{part}}$  is proportional to the volume of the fireball,  
 380  $N_{\text{part}}^{1/3}$  is a quantity proportional to a length scale, and therefore may account for the system-size dependence of the  $v_2$   
 381 values. In Fig. 12 we add to this comparison the results from the asymmetric Cu+Au collisions. This scaling brings  
 382 the  $v_2(p_T)$  results from the three collisions systems together across all centrality classes in this study.

383 In Fig. 13 the  $v_3(p_T)$  values are compared in Cu+Au and Au+Au collisions for events of the same centrality. Unlike  
 384 in the  $v_2(p_T)$  measurements, here the values of  $v_3(p_T)$  are ordered according to the initial triangularities  $\varepsilon_3$  listed  
 385 in Table I, with the Cu+Au results being larger than the Au+Au ones. In particular, in the most central 0%–10%  
 386 collisions  $\varepsilon_3$  in Cu+Au is about 50% larger than in Au+Au collisions, and a similar difference is observed in the  
 387  $v_3(p_T)$  values. In Fig. 14 the  $v_3(p_T)$  values are scaled by the initial  $\varepsilon_3$  eccentricity. A good agreement between the  
 388 different systems is observed at low  $p_T$  ( $\leq 2$  GeV/c), which indicates that the participant eccentricities obtained  
 389 in the Glauber model provide an adequate description of the fluctuating initial geometry. Additionally, we perform  
 390 scaling with  $\varepsilon_3 N_{\text{part}}^{1/3}$ , as was done for the  $v_2(p_T)$  measurements. The results of this scaling are shown in Fig. 15. In  
 391 this case, the measurement in Cu+Au and Au+Au collisions are in better agreement at high  $p_T$ , however at low  $p_T$

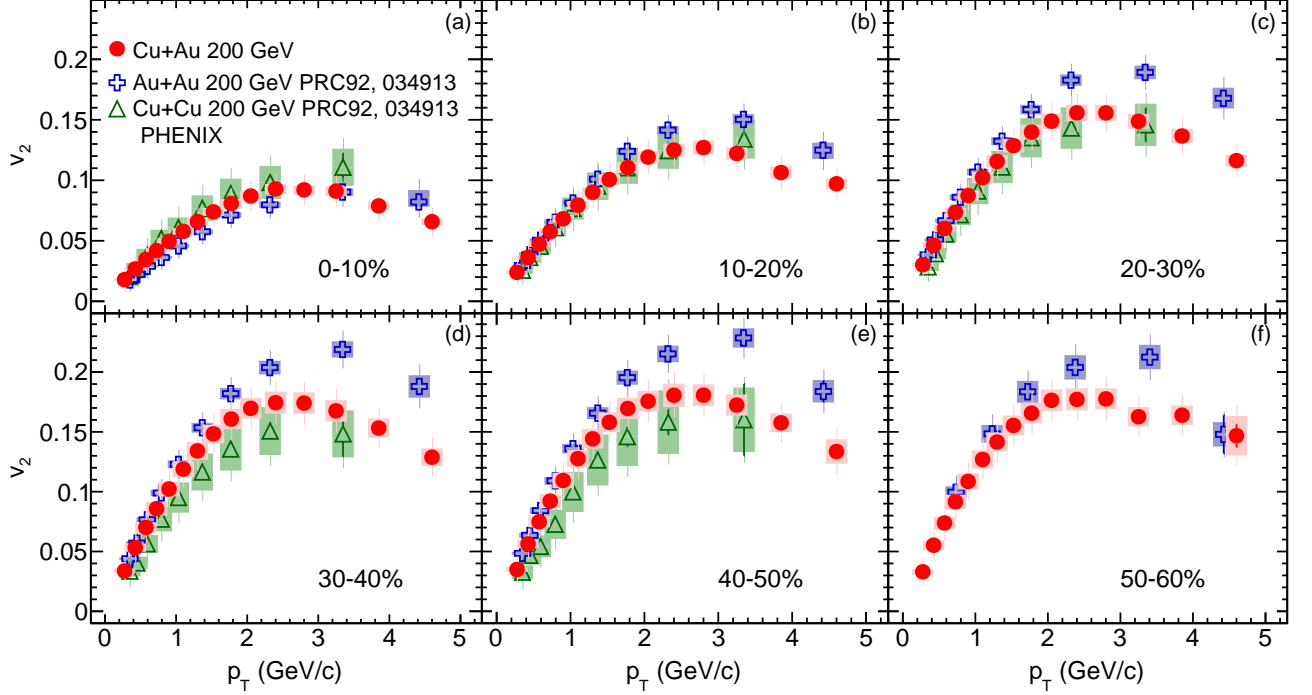


FIG. 10. (Color online) The second-order Fourier coefficients  $v_2(p_T)$  for charged hadrons measured at midrapidity in Cu+Au, Au+Au [12], and Cu+Cu [12] collisions at  $\sqrt{s_{NN}} = 200$  GeV. In each panel, the  $v_2(p_T)$  coefficients are compared for the same centrality class, as marked in the figure. The symbols represent the measured  $v_2(p_T)$  values, the error bars show the statistical uncertainties, and the shaded boxes indicate the systematic uncertainties.

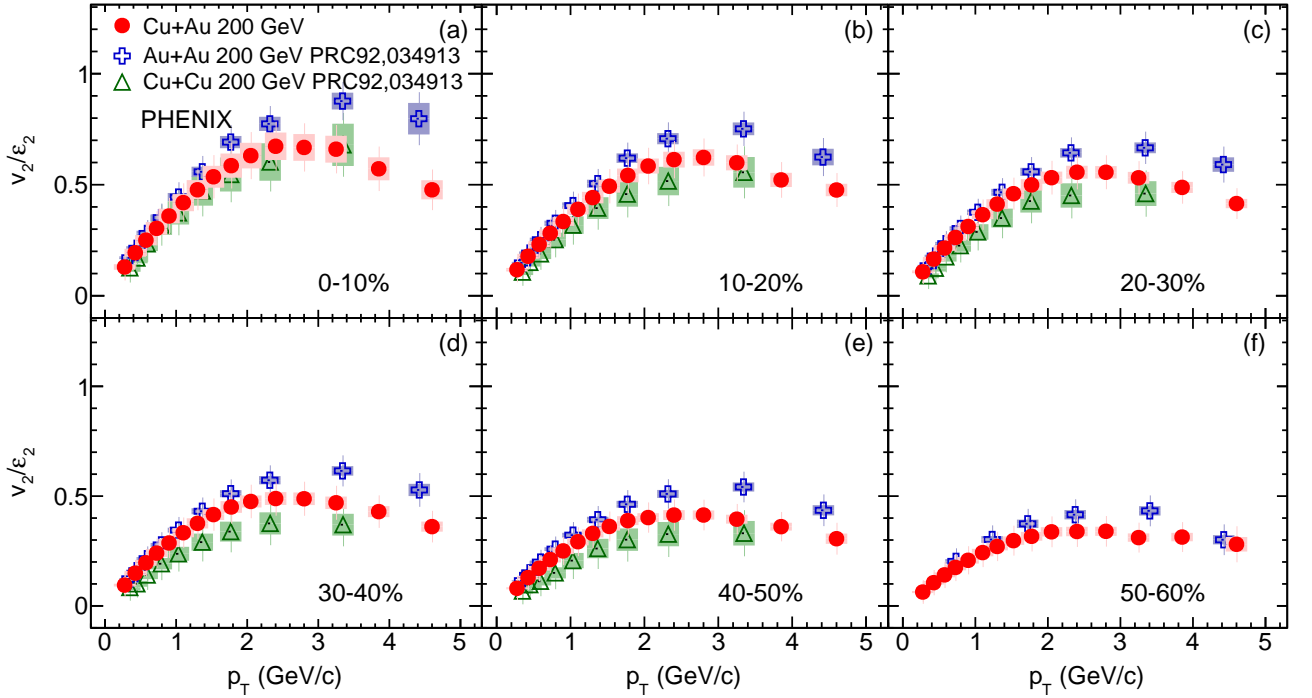


FIG. 11. (Color online) Scaled second-order Fourier coefficients  $v_2(p_T)/\epsilon_2$  for charged hadrons measured at midrapidity in Cu+Au, Au+Au [12], and Cu+Cu [12] collisions at  $\sqrt{s_{NN}} = 200$  GeV. In each panel, the  $v_2(p_T)$  values measured in the centrality classes marked in the figure, are scaled by the average second-order participant eccentricity  $\epsilon_2$  in the initial state of the collisions as determined by a MC Glauber calculation described in the text. The symbols represent the scaled  $v_2(p_T)/\epsilon_2$  values, the error bars show the statistical uncertainties, and the shaded boxes indicate the systematic uncertainties.

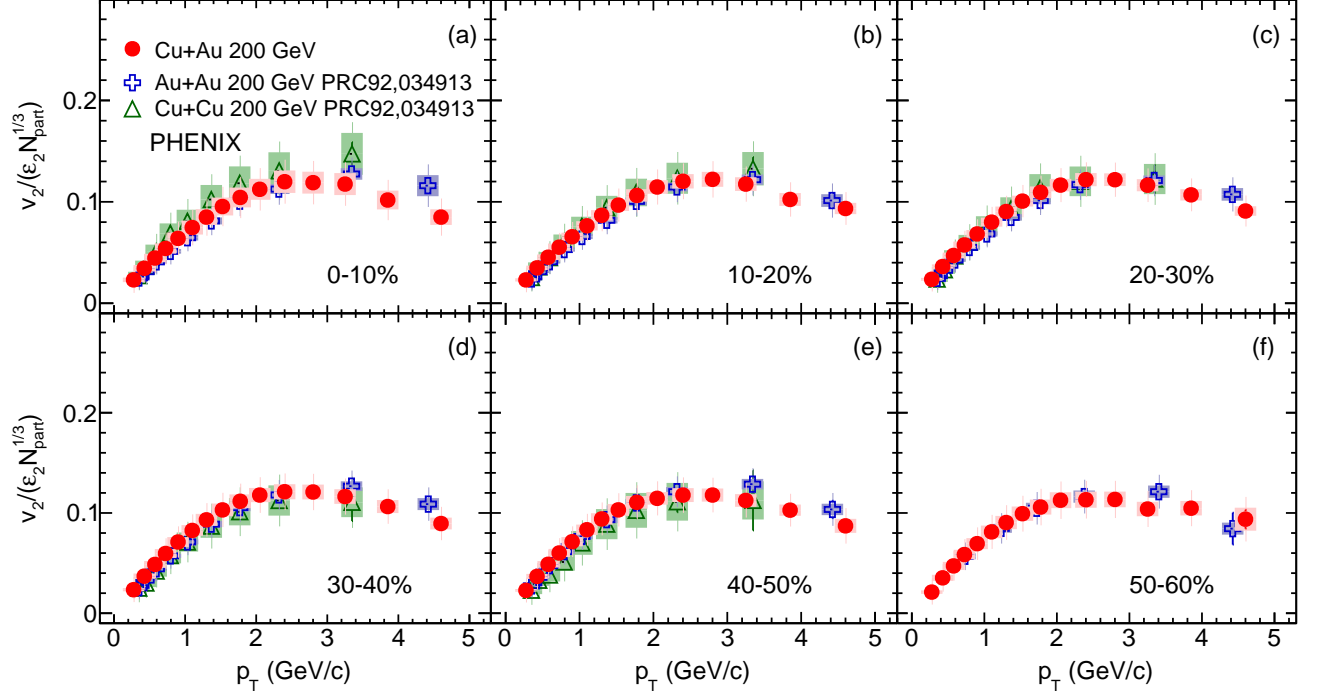


FIG. 12. (Color online) Scaled second-order Fourier coefficients  $v_2(p_T)/(\epsilon_2 N_{\text{part}}^{1/3})$  for charged hadrons measured at midrapidity in Cu+Au, Au+Au [12], and Cu+Cu [12] collisions at  $\sqrt{s_{NN}} = 200$  GeV. In each panel, the  $v_2(p_T)$  values measured in the centrality classes marked in the figure, are scaled by the average second-order participant eccentricity  $\epsilon_2$  in the initial state of the collisions as determined by a MC Glauber calculation described in the text, and the corresponding number of nucleon participants  $N_{\text{part}}^{1/3}$ . The symbols represent the scaled  $v_2(p_T)/(\epsilon_2 N_{\text{part}}^{1/3})$  values, the error bars show the statistical uncertainties, and the shaded boxes indicate the systematic uncertainties.

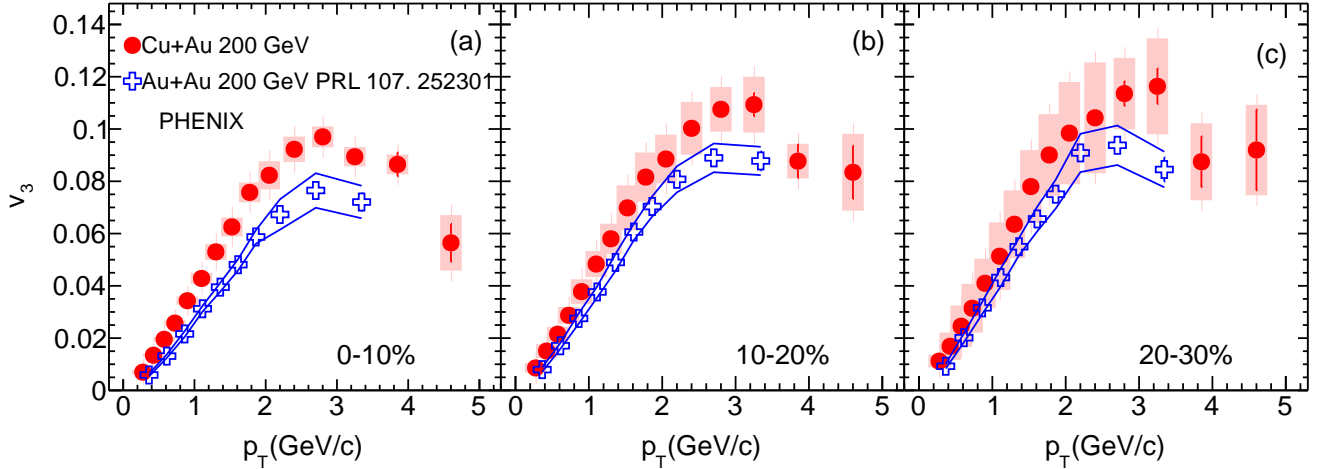


FIG. 13. (Color online) The third-order Fourier coefficients  $v_3(p_T)$  for charged hadrons measured at midrapidity in Cu+Au and Au+Au [22] collisions at  $\sqrt{s_{NN}} = 200$  GeV. In each panel, the  $v_3(p_T)$  coefficients are compared for the same centrality class, as marked in the figure. The symbols represent the measured  $v_3(p_T)$  values, the error bars show the statistical uncertainties, and the shaded boxes indicate the systematic uncertainties.

392 the  $v_3(p_T)/\varepsilon_3 N_{\text{part}}^{1/3}$  values are systematically higher for the Cu+Au system.

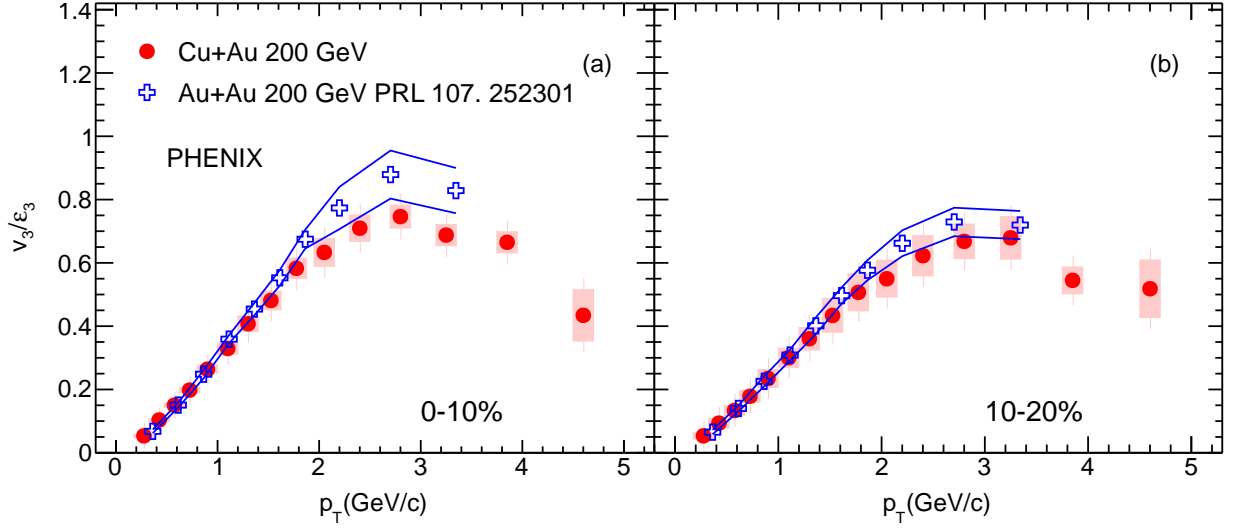


FIG. 14. (Color online) Scaled third-order Fourier coefficients  $v_3(p_T)/\varepsilon_3$  for charged hadrons measured at midrapidity in Cu+Au and Au+Au [22] collisions at  $\sqrt{s_{NN}} = 200$  GeV. In each panel, the  $v_3(p_T)$  values measured in the centrality classes marked in the figure, are scaled by the average third-order participant eccentricity  $\varepsilon_3$  in the initial state of the collisions as determined by a MC Glauber calculation described in the text. The symbols represent the scaled  $v_3(p_T)/\varepsilon_3$  values, and the error bars show the statistical uncertainties. The shaded boxes indicate the systematic uncertainties in the Cu+Au measurements, and the lines around the points marked with a cross show the systematic uncertainties in the Au+Au measurements.

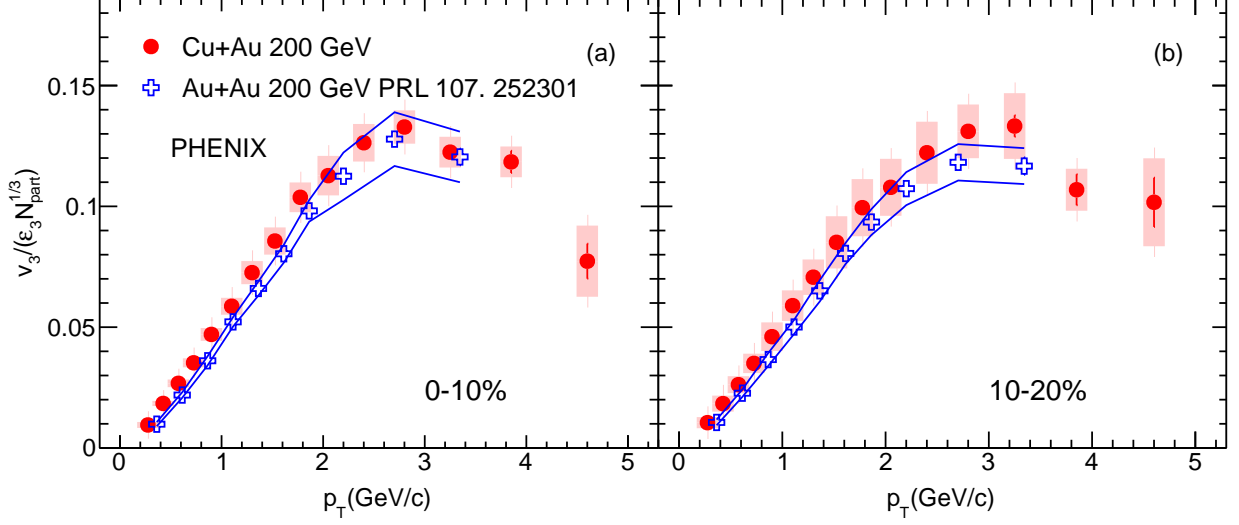


FIG. 15. (Color online) Scaled third-order Fourier coefficients  $v_3(p_T)/(\epsilon_3 N_{\text{part}}^{1/3})$  for charged hadrons measured at midrapidity in Cu+Au and Au+Au [22] collisions at  $\sqrt{s_{NN}} = 200$  GeV. In each panel, the  $v_3(p_T)$  values measured in the centrality classes marked in the figure, are scaled by the average third-order participant eccentricity  $\epsilon_3$  in the initial state of the collisions as determined by a MC Glauber calculation described in the text, and the corresponding number of nucleon participants  $N_{\text{part}}^{1/3}$ . The symbols represent the scaled  $v_3(p_T)/(\epsilon_3 N_{\text{part}}^{1/3})$  values, and the error bars show the statistical uncertainties. The shaded boxes indicate the systematic uncertainties in the Cu+Au measurements, and the lines around the points marked with a cross show the systematic uncertainties in the Au+Au measurements.

## D. Theory comparisons

### 1. Hydrodynamic calculations

Predictions from 3D+1 viscous hydrodynamic calculations are available [46]. At low  $p_T$  ( $< 1.0$  GeV/ $c$ ) directed flow is predicted to be in the hemisphere of the Cu side, while for high  $p_T$  ( $> 1.5$  GeV/ $c$ ) directed flow is predicted to be in the hemisphere on the Au side. Further, the bulk directed flow component from integration over  $p_T$  is predicted to be in the Cu-nucleus hemisphere. Due to the large systematic uncertainties and small value of  $v_1$  at small  $p_T$ , we can not reliably determine the sign of the  $v_1$  component at low  $p_T$ , or the sign of the bulk directed flow. At high  $p_T$  the measurement is in agreement with the directed flow being in the Au hemisphere, under the assumption that the spectator neutrons are deflected outward from the interaction region and aligned with the impact parameter vector. Ref. [46] shows the  $v_1$  with respect to the reaction plane (i.e. the impact parameter vector) for 20%–30% central Cu+Au collisions including particles within  $|\eta| < 1.0$ , and thus we cannot compare directly with our narrower rapidity selection. It is notable however, that the hydrodynamic results at  $p_T = 2$  GeV/ $c$  reach  $v_1 \approx 5\%$ , while the experimental data within  $|\eta| < 0.35$  are less than 2%.

The predictions for elliptic and triangular flow as a function of  $p_T$  are compared to the data in Fig. 16 and Fig. 17. Calculations with two different values of the specific viscosity  $\eta/s = 0.08$  and  $\eta/s = 0.16$  are shown. Our measurements in the 20%–30% centrality range are consistent with each of these values; for the most central 0%–5% events, a value of  $\eta/s = 0.08$  is closer to the data.

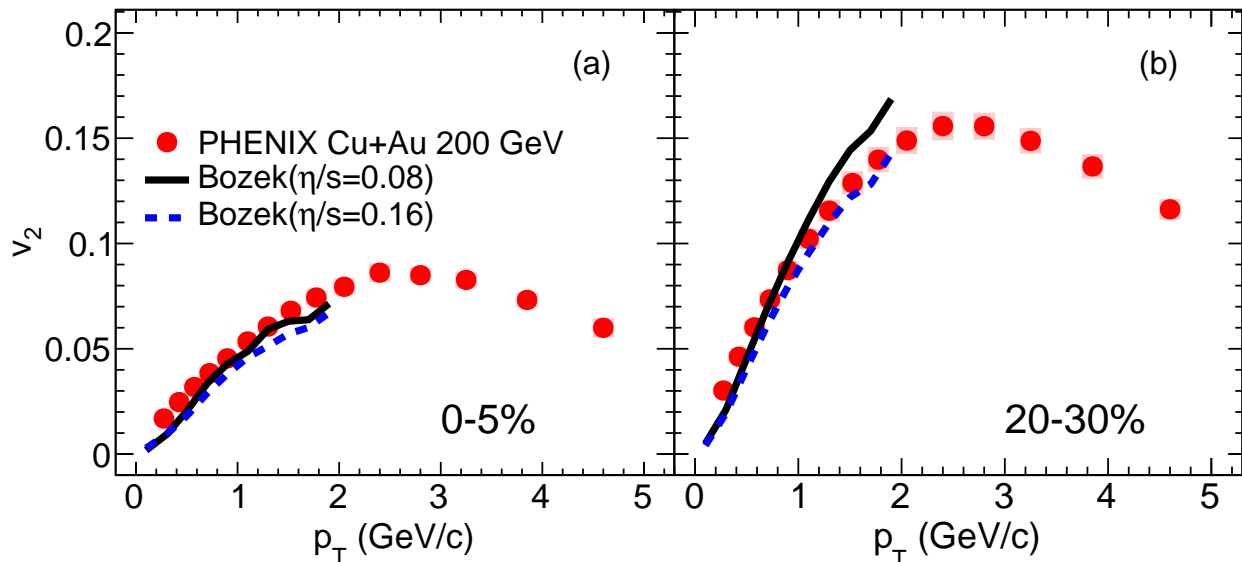


FIG. 16. (Color online) The second-order Fourier coefficients  $v_2(p_T)$  for charged hadrons measured at midrapidity in Cu+Au collisions at  $\sqrt{s_{NN}} = 200$  GeV in comparison to hydrodynamics calculations for the centrality classes marked in each panel. The symbols represent the measured  $v_2(p_T)$  values, the error bars show the statistical uncertainties, and the shaded boxes indicate the systematic uncertainties. The theoretical calculations, shown with the solid and dashed lines, are performed with two different values of the specific viscosity  $\eta/s$  marked in the figure.

### 2. AMPT

The A-Multiphase-Transport Model (AMPT) generator [47, 48] has been established as a useful tool in the study of flow observables in heavy-ion collisions [49]. Therefore, it is of interest to compare the measured  $v_1$ ,  $v_2$ , and  $v_3$  as a function of  $p_T$  with the corresponding quantities calculated using the AMPT model. To that end, we used AMPT v2.21 with string melting turned on to generate approximately 2 million minimum bias Cu+Au events at  $\sqrt{s_{NN}} = 200$  GeV, setting the partonic cross section alternately to  $\sigma_{\text{part}} = 1.5$  mb and 3.0 mb. In the default version of the model, initial conditions are generated using Monte Carlo Glauber with a *gray disk* approach to nucleon-nucleon interactions.

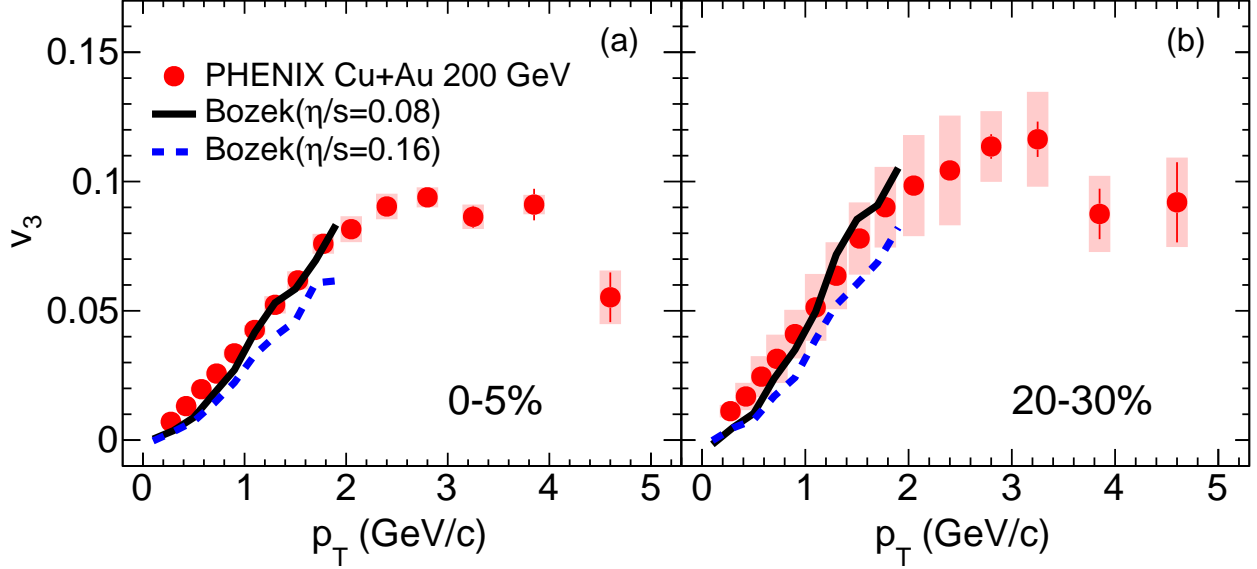


FIG. 17. (Color online) The third-order Fourier coefficients  $v_3(p_T)$  for charged hadrons measured at midrapidity in Cu+Au collisions at  $\sqrt{s_{NN}} = 200$  GeV in comparison to hydrodynamics calculations for the centrality classes marked in each panel. The symbols represent the measured  $v_3(p_T)$  values, the error bars show the statistical uncertainties, and the shaded boxes indicate the systematic uncertainties. The theoretical calculations, shown with the solid and dashed lines, are performed with two different values of the specific viscosity  $\eta/s$  marked in the figure.

417 However, in this study we utilize a modified *black disk* Glauber model with a fixed nucleon-nucleon inelastic cross  
 418 section of 42 mb, as used in Ref. [49].

419 Following the method of [49], Fourier coefficients  $v_1$ ,  $v_2$ , and  $v_3$  are calculated for unidentified charged hadrons within  
 420  $|\eta| < 0.35$ , with respect to the corresponding participant planes  $\Psi_1$ ,  $\Psi_2$ , and  $\Psi_3$ . These plane angles are computed  
 421 for each event from the initial coordinates of nucleon participants with a Gaussian smearing of width  $\sigma = 0.4$  fm.

422 The  $v_2(p_T)$  and  $v_3(p_T)$  results shown in Fig. 18 and Fig. 19 are well reproduced by the model for  $p_T < 1$  GeV/c.  
 423 The comparison with the data indicates that the 3.0 mb partonic cross section gives a better description of the system  
 424 dynamics.

425 However, the calculation of  $v_1$  and its comparison with experimental data is less straightforward. Because the  
 426 experimentally measured Cu spectator neutron orientation is unknown, we calculate the  $v_1$  values with respect to  
 427 the impact parameter vector  $\vec{b}$  pointing in the direction of the Cu nucleus as well as with respect to  $\Psi_1$ , the overlap  
 428 region calculated as previously described. Because the calculation is done in the participant center-of-mass frame,  
 429 weighting all participants equally yields exactly  $\varepsilon_1 = 0$  and hence no direction for  $\Psi_1$ . There are various suggestions  
 430 in the literature for weighting with  $r^2$  and  $r^3$  [50, 51], and in this study we choose to use  $r^2$ .

431 In addition, we have considered two different Monte Carlo Glauber initial conditions, one with black disk (BD)  
 432 nucleons and one with gray disk (GD) nucleons, thus varying the diffuseness of the nucleon-nucleon interaction radius.  
 433 Figure 20 shows results for Cu+Au collisions within the 30%-40% centrality selection on the relative distribution of  
 434  $\Psi_1$  to  $\vec{b}$  pointing the direction of the Cu nucleus. Panel (a) is for the BD case and Panel (b) the GD case. This small  
 435 difference in the treatment of initial geometry completely re-orientates the  $\Psi_1$  vector. The lower panels show the AMPT  
 436 midrapidity particle  $v_1$  as a function of  $p_T$  relative to  $\Psi_1$  and  $\vec{b}$  again the BD and GD implementation. It is interesting  
 437 to note that in the GD case where the two results agree, the prediction is for low  $p_T$  particles moving in the direction  
 438 of the Au nucleus and the high  $p_T$  particles in the direction of the Cu nucleus (opposite to the previously discussed  
 439 hydrodynamic prediction).

440 We note that it is currently unknown whether the spectator neutrons bend toward or away from the interaction  
 441 overlap region between the nuclei, and whether they are oriented along the impact parameter vector  $\vec{b}$ , along the vector  
 442  $\Psi_1$  determined by the initial energy density in the overlap region, or some other vector. In fact, it is conceivable that  
 443 spectators very close to the overlap region have a different behavior from spectators far away from the overlap. These  
 444 ambiguities need resolution before a more direct theory to data comparison can be made.

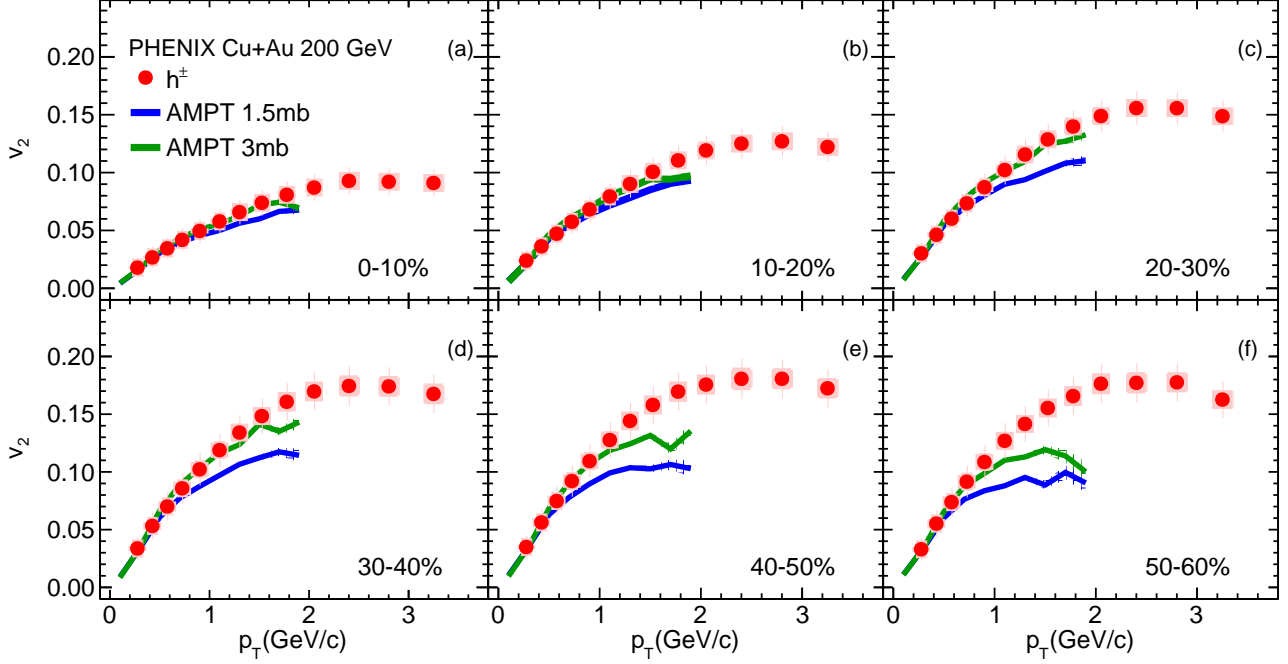


FIG. 18. (Color online) The second-order Fourier coefficients  $v_2(p_T)$  for charged hadrons measured at midrapidity in Cu+Au collisions at  $\sqrt{s_{NN}} = 200$  GeV in comparison to AMPT model calculation for the centrality classes marked in each panel. The symbols represent the measured  $v_2(p_T)$  values, the error bars show the statistical uncertainties, and the shaded boxes indicate the systematic uncertainties. For the theoretical calculations, which are shown with lines, only statistical uncertainties are plotted.

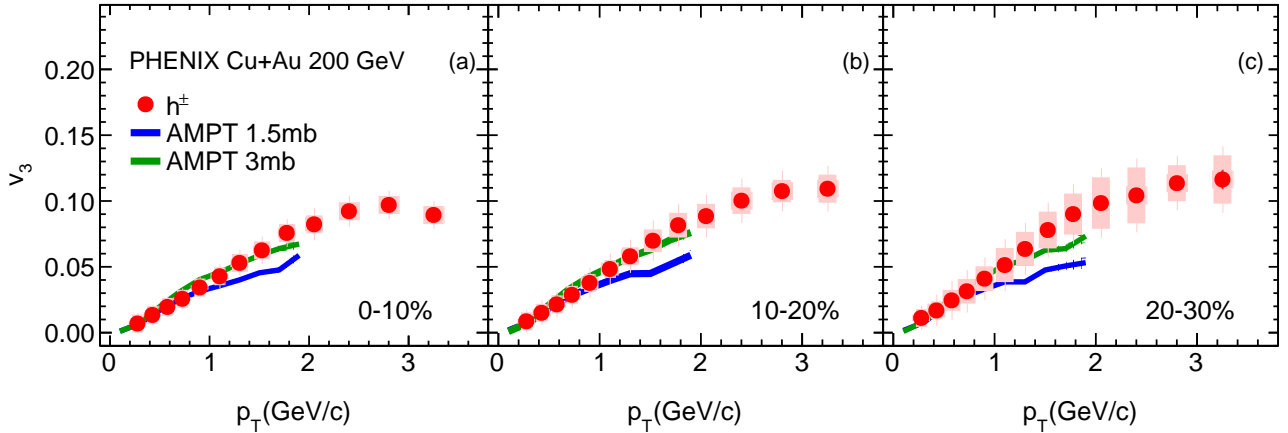


FIG. 19. (Color online) The third-order Fourier coefficients  $v_3(p_T)$  for charged hadrons measured at midrapidity in Cu+Au collisions at  $\sqrt{s_{NN}} = 200$  GeV in comparison to AMPT model calculation for the centrality classes marked in each panel. The symbols represent the measured  $v_3(p_T)$  values, the error bars show the statistical uncertainties, and the shaded boxes indicate the systematic uncertainties. For the theoretical calculations, which are shown with lines, only statistical uncertainties are plotted.

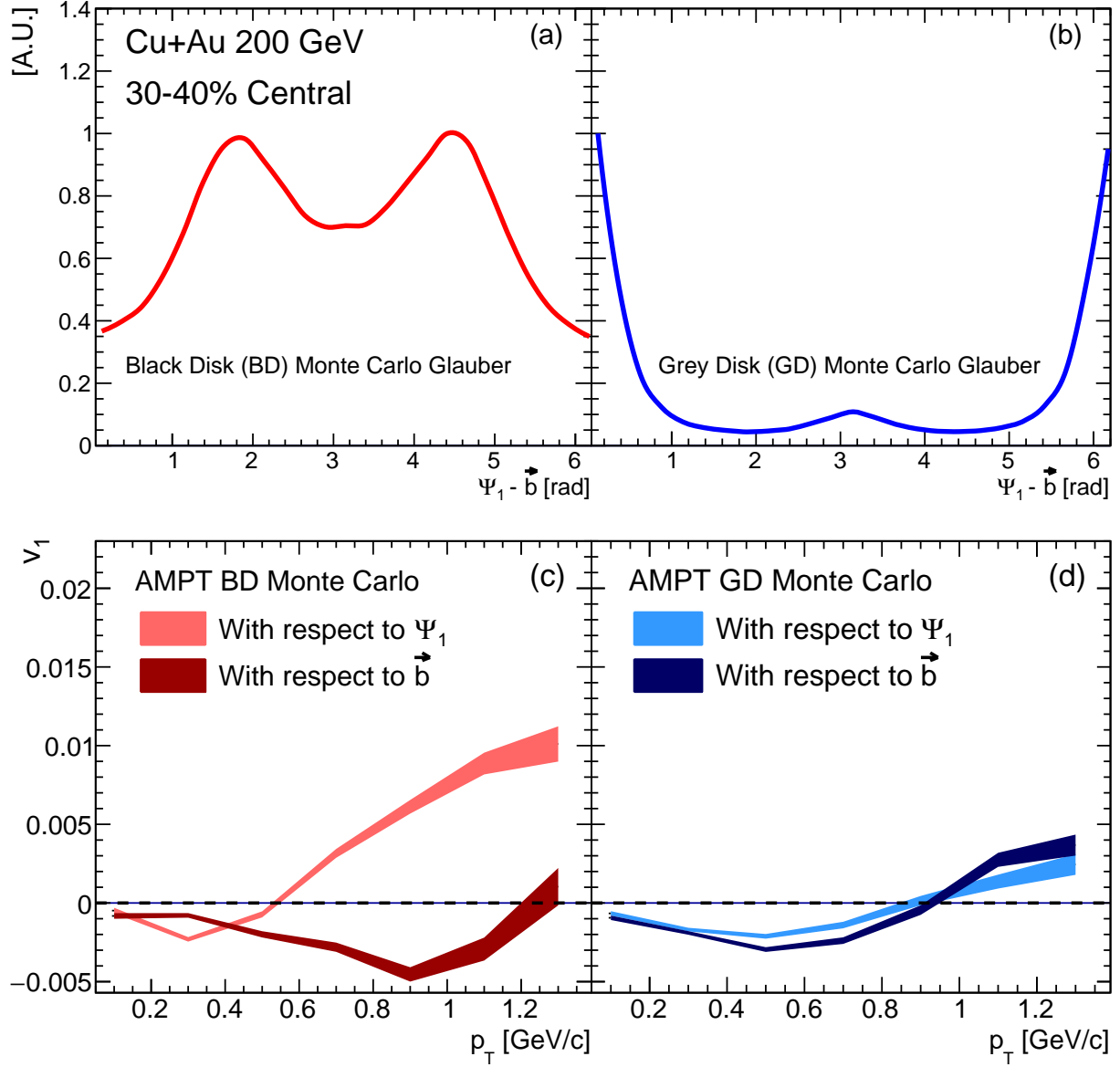


FIG. 20. (Color online) The top panels show the maximum-normalized distribution of first-order participant plane angle  $\Psi_1$  computed from the initial coordinates of participant nucleons determined with (a) black disk, and (b) gray disk Monte Carlo Glauber simulations. The bottom panels show AMPT  $v_1$  computed with respect to the impact parameter  $\vec{b}$ , and  $\Psi_1$  using (c) black disk and (d) gray disk Monte Carlo for the initial conditions.

#### IV. SUMMARY

445 Anisotropic flow coefficients for inclusive charged particles and identified hadrons  $\pi^\pm$ ,  $K^\pm$ ,  $p$ , and  $\bar{p}$  produced in  
 446 Cu+Au collisions at  $\sqrt{s_{NN}} = 200$  GeV have been measured by the PHENIX experiment at RHIC using event plane  
 447 techniques. The  $v_1$ ,  $v_2$ , and  $v_3$  measurements were performed at midrapidity as a function of transverse momentum  
 448  $p_T$  over a broad range of collision centralities. Mass ordering was observed for low  $p_T$  in the identified particle  
 449 measurements, as predicted by hydrodynamics.

450 A system size comparison was performed for the inclusive charged particles using previous PHENIX measurements  
 451 at  $\sqrt{s_{NN}} = 200$  GeV of  $v_2(p_T)$  in Cu+Cu and Au+Au collisions, and  $v_3(p_T)$  in Au+Au collisions. The elliptic and  
 452 triangular flow measurements between different systems and centrality selections were found to scale with the product  
 453 of the initial participant eccentricity and the third root of the number of nucleon participants  $\varepsilon_n N_{\text{part}}^{1/3}$ . The system  
 454 size dependence of the  $v_3(p_T)$  values could also be described by participant eccentricity  $\varepsilon_3$  scaling alone.

455 The inclusive charged-particle measurements were compared to theoretical predictions. In the  $v_1$  measurement,  
 456 we observed negative values at high  $p_T$ , indicating that hadrons are emitted in the transverse plane preferentially  
 457 in the hemisphere of the spectators from the Au nucleus, assuming that they moved outward from the interaction  
 458 region and are aligned with the impact parameter vector. The AMPT transport model calculations were found to  
 459 be in agreement with the magnitude of the measured  $v_1(p_T)$  signals, but having the opposite sign. At low  $p_T$  ( $< 1$   
 460 GeV/ $c$ ) AMPT provides a reasonable description of the triangular flow in all measured centrality classes that cover the  
 461 0%–30% range, and the elliptic flow measurements in the 0%–60% range. Event-by-event hydrodynamics calculations  
 462 with specific viscosity in the range  $\eta/s = 0.08 - 0.16$  reproduce the measured  $v_2(p_T)$  and  $v_3(p_T)$  values.  
 463

#### ACKNOWLEDGMENTS

464 We thank the staff of the Collider-Accelerator and Physics Departments at Brookhaven National Laboratory and  
 465 the staff of the other PHENIX participating institutions for their vital contributions. We acknowledge support from  
 466 the Office of Nuclear Physics in the Office of Science of the Department of Energy, the National Science Foundation,  
 467 Abilene Christian University Research Council, Research Foundation of SUNY, and Dean of the College of Arts  
 468 and Sciences, Vanderbilt University (U.S.A), Ministry of Education, Culture, Sports, Science, and Technology and  
 469 the Japan Society for the Promotion of Science (Japan), Conselho Nacional de Desenvolvimento Científico e Tec-  
 470 nológico and Fundação de Amparo à Pesquisa do Estado de São Paulo (Brazil), Natural Science Foundation of China  
 471 (P. R. China), Croatian Science Foundation and Ministry of Science, Education, and Sports (Croatia), Ministry of Ed-  
 472 ucation, Youth and Sports (Czech Republic), Centre National de la Recherche Scientifique, Commissariat à l'Énergie  
 473 Atomique, and Institut National de Physique Nucléaire et de Physique des Particules (France), Bundesministerium  
 474 für Bildung und Forschung, Deutscher Akademischer Austausch Dienst, and Alexander von Humboldt Stiftung (Ger-  
 475 many), National Science Fund, OTKA, Károly Róbert University College, and the Ch. Simonyi Fund (Hungary),  
 476 Department of Atomic Energy and Department of Science and Technology (India), Israel Science Foundation (Israel),  
 477 Basic Science Research Program through NRF of the Ministry of Education (Korea), Physics Department, Lahore  
 478 University of Management Sciences (Pakistan), Ministry of Education and Science, Russian Academy of Sciences,  
 479 Federal Agency of Atomic Energy (Russia), VR and Wallenberg Foundation (Sweden), the U.S. Civilian Research and  
 480 Development Foundation for the Independent States of the Former Soviet Union, the Hungarian American Enterprise  
 481 Scholarship Fund, and the US-Israel Binational Science Foundation.  
 482

- 
- 483 [1] S. Voloshin and Y. Zhang, “Flow study in relativistic nuclear collisions by Fourier expansion of azimuthal particle distri-  
 484 butions,” *Z. Phys. C* **70**, 665 (1996).  
 485 [2] K. Adcox *et al.* (PHENIX Collaboration), “Formation of dense partonic matter in relativistic nucleus-nucleus collisions at  
 486 RHIC: Experimental evaluation by the PHENIX Collaboration,” *Nucl. Phys. A* **757**, 184 (2005).  
 487 [3] J. Adams *et al.* (STAR Collaboration), “Experimental and theoretical challenges in the search for the quark gluon plasma:  
 488 The STAR Collaboration’s critical assessment of the evidence from RHIC collisions,” *Nucl. Phys. A* **757**, 102 (2005).  
 489 [4] B. B. Back *et al.*, “The PHOBOS perspective on discoveries at RHIC,” *Nucl. Phys. A* **757**, 28 (2005).  
 490 [5] E. V. Shuryak, “What RHIC experiments and theory tell us about properties of quark-gluon plasma?” *Proceedings, RBRC*  
 491 *Workshop, Brookhaven, Upton, USA, May 14-15, 2004*, *Nucl. Phys. A* **750**, 64 (2005).  
 492 [6] M. Gyulassy and L. McLerran, “New forms of QCD matter discovered at RHIC,” *Proceedings, RBRC Workshop,*  
 493 *Brookhaven, Upton, USA, May 14-15, 2004*, *Nucl. Phys. A* **750**, 30 (2005).  
 494 [7] J. Barrette *et al.* (E877), “Energy and charged particle flow in a 10.8 A/GeV/ $c$  Au+Au collisions,” *Phys. Rev. C* **55**, 1420  
 495 (1997), [Erratum: *Phys. Rev. C* **56**, 2336(E)(1997)].

- [8] C. Alt *et al.* (NA49 Collaboration), “Directed and elliptic flow of charged pions and protons in Pb + Pb collisions at 40-A GeV and 158-A-GeV,” *Phys. Rev. C* **68**, 034903 (2003).
- [9] C. Adler *et al.* (STAR Collaboration), “Elliptic flow from two and four particle correlations in Au+Au collisions at  $\sqrt{s_{NN}} = 130$  GeV,” *Phys. Rev. C* **66**, 034904 (2002).
- [10] L. Adamczyk *et al.* (STAR Collaboration), “Elliptic flow of identified hadrons in Au+Au collisions at  $\sqrt{s_{NN}} = 7.7$ -62.4 GeV,” *Phys. Rev. C* **88**, 014902 (2013).
- [11] B. Alver *et al.* (PHOBOS Collaboration), “System size, energy, pseudorapidity, and centrality dependence of elliptic flow,” *Phys. Rev. Lett.* **98**, 242302 (2007).
- [12] A. Adare *et al.* (PHENIX), “Systematic Study of Azimuthal Anisotropy in Cu+Cu and Au+Au Collisions at  $\sqrt{s_{NN}} = 62.4$  and 200 GeV,” *Phys. Rev. C* **92**, 034913 (2015).
- [13] K. Aamodt *et al.* (ALICE Collaboration), “Elliptic flow of charged particles in Pb-Pb collisions at 2.76 TeV,” *Phys. Rev. Lett.* **105**, 252302 (2010).
- [14] G. Aad *et al.* (ATLAS Collaboration), “Measurement of the pseudorapidity and transverse momentum dependence of the elliptic flow of charged particles in lead-lead collisions at  $\sqrt{s_{NN}}=2.76$  TeV with the ATLAS detector,” *Phys. Lett. B* **707**, 330 (2012).
- [15] S. Chatrchyan *et al.* (CMS Collaboration), “Measurement of the elliptic anisotropy of charged particles produced in PbPb collisions at  $\sqrt{s_{NN}}=2.76$  TeV,” *Phys. Rev. C* **87**, 014902 (2013).
- [16] B. B. Back *et al.* (PHOBOS Collaboration), “Energy dependence of directed flow over a wide range of pseudorapidity in Au + Au collisions at RHIC,” *Phys. Rev. Lett.* **97**, 012301 (2006).
- [17] L. Adamczyk *et al.* (STAR Collaboration), “Beam-Energy Dependence of the Directed Flow of Protons, Antiprotons, and Pions in Au+Au Collisions,” *Phys. Rev. Lett.* **112**, 162301 (2014).
- [18] B. Abelev *et al.* (ALICE Collaboration), “Directed Flow of Charged Particles at Midrapidity Relative to the Spectator Plane in Pb-Pb Collisions at  $\sqrt{s_{NN}}=2.76$  TeV,” *Phys. Rev. Lett.* **111**, 232302 (2013).
- [19] D. H. Rischke, Horst Stoecker, W. Greiner, and B. L. Friman, “Phase Transition From Hadron Gas to Quark Gluon Plasma: Influence of the Stiffness of the Nuclear Equation of State,” *J. Phys. G* **14**, 191 (1988).
- [20] B. Alver and G. Roland, “Collision geometry fluctuations and triangular flow in heavy-ion collisions,” *Phys. Rev. C* **81**, 054905 (2010), [Erratum: *Phys. Rev. C* 82,039903(E)(2010)].
- [21] A. Adare *et al.* (PHENIX), “Measurement of the higher-order anisotropic flow coefficients for identified hadrons in Au+Au collisions at  $\sqrt{s_{NN}} = 200$  GeV,” *Phys. Rev. C* **93**, 051902 (2016).
- [22] A. Adare *et al.* (PHENIX Collaboration), “Measurements of Higher-Order Flow Harmonics in Au+Au Collisions at  $\sqrt{s_{NN}}=200$  GeV,” *Phys. Rev. Lett.* **107**, 252301 (2011).
- [23] L. Adamczyk *et al.* (STAR Collaboration), “Third Harmonic Flow of Charged Particles in Au+Au Collisions at  $\sqrt{s_{NN}} = 200$  GeV,” *Phys. Rev. C* **88**, 014904 (2013).
- [24] K. Aamodt *et al.* (ALICE Collaboration), “Higher harmonic anisotropic flow measurements of charged particles in Pb-Pb collisions at  $\sqrt{s_{NN}}=2.76$  TeV,” *Phys. Rev. Lett.* **107**, 032301 (2011).
- [25] G. Aad *et al.* (ATLAS Collaboration), “Measurement of the azimuthal anisotropy for charged particle production in  $\sqrt{s_{NN}}=2.76$  TeV lead-lead collisions with the ATLAS detector,” *Phys. Rev. C* **86**, 014907 (2012).
- [26] S. Chatrchyan *et al.* (CMS Collaboration), “Measurement of higher-order harmonic azimuthal anisotropy in PbPb collisions at  $\sqrt{s_{NN}} = 2.76$  TeV,” *Phys. Rev. C* **89**, 044906 (2014).
- [27] Bjorn Schenke, Sangyong Jeon, and Charles Gale, “Higher flow harmonics from (3+1)D event-by-event viscous hydrodynamics,” *Phys. Rev. C* **85**, 024901 (2012).
- [28] Sean Gavin and G. Moschelli, “Fluctuation Probes of Early-Time Correlations in Nuclear Collisions,” *Phys. Rev. C* **85**, 014905 (2012).
- [29] L. X. Han, G. L. Ma, Y. G. Ma, X. Z. Cai, J. H. Chen, S. Zhang, and C. Zhong, “Initial fluctuation effect on harmonic flow in high-energy heavy-ion collisions,” *Phys. Rev. C* **84**, 064907 (2011).
- [30] G. Y. Qin, H. Petersen, S. A. Bass, and B. Muller, “Translation of collision geometry fluctuations into momentum anisotropies in relativistic heavy-ion collisions,” *Phys. Rev. C* **82**, 064903 (2010).
- [31] Zhi Qiu and U. W. Heinz, “Event-by-event shape and flow fluctuations of relativistic heavy-ion collision fireballs,” *Phys. Rev. C* **84**, 024911 (2011).
- [32] Pilar Staig and E. Shuryak, “The Fate of the Initial State Fluctuations in Heavy Ion Collisions. III The Second Act of Hydrodynamics,” *Phys. Rev. C* **84**, 044912 (2011).
- [33] K. Adcox *et al.* (PHENIX Collaboration), “PHENIX detector overview,” *Nucl. Instrum. Methods Phys. Res., Sec. A* **499**, 469 (2003).
- [34] C. Adler, A. Denisov, E. Garcia, M. Murray, H. Strobele, and S. White, “The RHIC zero-degree calorimeters,” *Nucl. Instrum. Methods Phys. Res., Sec. A* **499**, 433 (2003).
- [35] D. Ben-Tzvi and M.B. Sandler, “A combinatorial hough transform,” *Pattern Recognition Letters* **11**, 167 (1990).
- [36] A. Adare *et al.* (PHENIX Collaboration), “Spectra and ratios of identified particles in Au+Au and d+Au collisions at  $\sqrt{s_{NN}}=200$  GeV,” *Phys. Rev. C* **88**, 024906 (2013).
- [37] M. Aizawa *et al.* (PHENIX Collaboration), “PHENIX central arm particle ID detectors,” *Nucl. Instrum. Meth. Phys. Res., Sect. A* **499**, 508–520 (2003).
- [38] A. Adare *et al.* (PHENIX Collaboration), “Deviation from quark-number scaling of the anisotropy parameter  $v_2$  of pions, kaons, and protons in Au+Au collisions at  $\sqrt{s_{NN}} = 200$  GeV,” *Phys. Rev. C* **85**, 064914 (2012).
- [39] A. M. Poskanzer and S. A. Voloshin, “Methods for analyzing anisotropic flow in relativistic nuclear collisions,” *Phys. Rev. C* **58**, 1671 (1998).

- 560 [40] M. Alvioli and M. Strikman, “Beam Fragmentation in Heavy Ion Collisions with Realistically Correlated Nuclear Config-  
561 urations,” Phys. Rev. **C83**, 044905 (2011).
- 562 [41] S. Afanasiev *et al.* (PHENIX Collaboration), “Systematic Studies of Elliptic Flow Measurements in Au+Au Collisions at  
563  $\sqrt{s} = 200$  GeV,” Phys. Rev. C **80**, 024909 (2009).
- 564 [42] B. Abelev *et al.* (ALICE Collaboration), “Directed Flow of Charged Particles at Midrapidity Relative to the Spectator  
565 Plane in Pb-Pb Collisions at  $\sqrt{s_{NN}}=2.76$  TeV,” Phys. Rev. Lett. **111**, 232302 (2013).
- 566 [43] B. Alver *et al.* (PHOBOS Collaboration), “System size, energy, pseudorapidity, and centrality dependence of elliptic flow,”  
567 Phys. Rev. Lett. **98**, 242302 (2007).
- 568 [44] S.J. Sanders M.L. Miller, K. Reygers and P. Steinberg, “Glauber modeling in high-energy nuclear collisions,” Ann. Rev.  
569 Nucl. Part. Sci. **57**, 205 (2007).
- 570 [45] A. Adare *et al.* (PHENIX Collaboration), “Scaling properties of azimuthal anisotropy in Au+Au and Cu+Cu collisions at  
571  $\sqrt{s} = 200$  GeV,” Phys. Rev. Lett. **98**, 162301 (2007).
- 572 [46] P. Bozek, “Event-by-event viscous hydrodynamics for Cu-Au collisions at 200GeV,” Phys. Lett. B **717**, 287 (2012).
- 573 [47] Zi-Wei Lin, Che Ming Ko, Bao-An Li, Bin Zhang, and Subrata Pal, “A Multi-phase transport model for relativistic heavy  
574 ion collisions,” Phys. Rev. C **72**, 064901 (2005).
- 575 [48] Lie-Wen Chen and Che Ming Ko, “Anisotropic flow in Cu+Au collisions at  $\sqrt{s_{NN}} = 200$  GeV,” Phys. Rev. C **73**, 014906  
576 (2006).
- 577 [49] J. D. Orjuela Koop, A. Adare, D. McGlinchey, and J. L. Nagle, “Azimuthal anisotropy relative to the participant plane  
578 from a multiphase transport model in central p + Au , d + Au , and  $^3\text{He} + \text{Au}$  collisions at  $\sqrt{s_{NN}} = 200$  GeV,” Phys.  
579 Rev. **C 92**, 054903 (2015).
- 580 [50] Fernando G. Gardim, Frederique Grassi, Yojiro Hama, M. Luzum, and J.-Y. Ollitrault, “Directed flow at mid-rapidity in  
581 event-by-event hydrodynamics,” Phys. Rev. C **83**, 064901 (2011).
- 582 [51] D. Teaney and Li Yan, “Triangularity and Dipole Asymmetry in Heavy Ion Collisions,” Phys. Rev. C **83**, 064904 (2011).